North American lithospheric discontinuity structure imaged by *Ps* and *Sp* receiver functions

David L. Abt,[1,2] Karen M. Fischer,[1] Scott W. French,[1,3] Heather A. Ford,[1] Huaiyu Yuan,[4] and Barbara Romanowicz[4]

Received 26 August 2009; revised 1 March 2010; accepted 22 April 2010; published 23 September 2010.

[1] *Sp* and *Ps* converted seismic waves at 93 permanent seismic stations are used to image upper mantle velocity discontinuities across the contiguous United States and portions of southeast Canada and northwest Mexico. Receiver functions are calculated with frequency-domain deconvolution and migrated with 1D models that account for variations in crustal structure and mantle velocities between stations. Strong positive *Ps* phases from the Moho are observed and agree well with previous crustal thickness estimates. In the tectonically active western U.S., high amplitude, negative *Sp* phases are interpreted as the lithosphere-asthenosphere boundary (LAB) at depths of 51–104 km. These phases indicate a large and rapid LAB velocity gradient and are consistent with an anomalously hot asthenosphere that is rich in water or contains partial melt. In the regions of the Phanerozoic southern and eastern U.S where *Sp* phases are interpretable as the LAB, the discontinuity lies at depths of 75–111 km and is also too sharp to be explained by temperature alone. In contrast, no *Sp* phases are observed at depths comparable to the base of the thick high velocity lithosphere that lies beneath cratonic North America and certain portions of the Phanerozoic eastern U.S. At these stations, negative *Sp* phases occur at depths of 59–113 km and are interpreted as the top of a low velocity zone internal to the lithosphere. The absence of an observable LAB discontinuity in regions of thick lithosphere indicates that the LAB velocity gradient is distributed over more than 50–70 km in depth and is consistent with a purely thermal boundary.

Citation: Abt, D. L., K. M. Fischer, S. W. French, H. A. Ford, H. Yuan, and B. Romanowicz (2010), North American lithospheric discontinuity structure imaged by *Ps* and *Sp* receiver functions, *J. Geophys. Res.*, *115*, B09301, doi:10.1029/2009JB006914.

1. Introduction

[2] Determining the location and physical properties of the lithosphere-asthenosphere boundary (LAB) is essential to our understanding of plate tectonics and the evolution of the Earth. More specifically, the presence of variations in the depth and character of the LAB across and within different tectonic environments (e.g., cratons, passive margins, extensional provinces, subduction zones) could provide insight into the growth and stability of lithospheric plates as well as the mechanism(s) responsible for their plate-like behavior. Ancient cratonic regions are expected to contain thick lithospheric roots that are rheologically strong with a chemical buoyancy that counteracts their cold temperatures [e.g., *Jordan*, 1978; *Jordan*, 1988; *Anderson*, 1989; *Boyd*, 1989; *Griffin et al.*, 1999; *Sleep*, 2005], making them stable relative to the surrounding upper mantle [e.g., *Pearson et al.*, 1995; *Carlson et al.*, 1999; *Shapiro et al.*, 1999]. A key question that we will address in this paper is whether the properties of the cratonic LAB fundamentally differ from the LAB in regions that have experienced more recent tectonic activity.

[3] The North American lithosphere has a rich tectonic history that includes the progressive accretion of lithotectonic terranes around Archean cratons (e.g., Superior, Wyoming, Hearne, Slave) during the Proterozoic, successful and failed rifting events, multiple episodes of subduction, and current large-scale extension in the Basin and Range province (Figure 1) [e.g., *Rivers*, 1997; *Karlstrom and Humphreys*, 1998; *Chulick and Mooney*, 2002; *Griffin et al.*, 2004]. Numerous global and regional tomographic studies [e.g., *Grand and Helmberger*, 1984; *Grand*, 1994; *van der Lee and Nolet*, 1997; *van der Lee*, 2002; *Li et al.*, 2003; *Godey et al.*, 2004; *Marone et al.*, 2007; *Xue and Allen*, 2007; *Nettles and Dziewonski*, 2008; *Roth et al.*, 2008; *Yuan and Romanowicz*, 2010] have interpreted lithospheric thickness across North America from relatively long wavelength images of velocity

[1]Department of Geological Sciences, Brown University, Providence, Rhode Island, USA.
[2]Now at ExxonMobil Exploration Company, Houston, Texas, USA.
[3]Now at Department of Earth and Planetary Science, University of California, Berkeley, California, USA.
[4]Berkeley Seismological Laboratory, University of California, Berkeley, California, USA.

0148-0227/10/2009JB006914

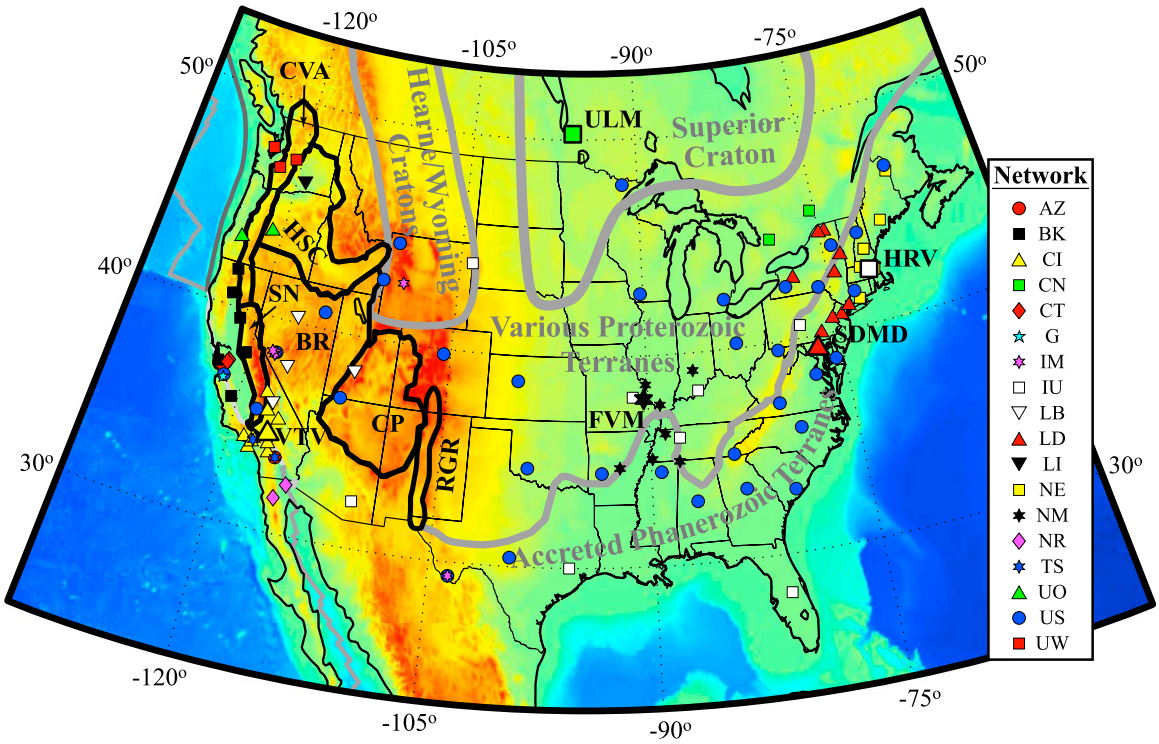

Figure 1. Permanent seismic stations used in this study, topography, and tectonic boundaries. The stations are distinguished by network, and the five stations presented as detailed examples in section 4.2 (VTV, ULM, HRV, FVM, and SDMD) are highlighted. See Table 1 for network information and auxiliary material Figure S1 for all station locations. Major boundaries between Archean, Proterozoic, and Phanerozoic lithotectonic terranes are shown schematically with thick gray lines [*Rivers*, 1997; *Chulick and Mooney*, 2002; *Griffin et al.*, 2004], and the Rio Grande Rift (RGR), Colorado Plateau (CP), Basin and Range (BR), High Lava Plains/Snake River Plain/Columbia Plateau (HSC), Cascades volcanic arc (CA), and Sierra Nevada batholith (SN) are shown with thick black lines [*Freeman and Johnson*, 1946]. Topography and bathymetry are from *Smith and Sandwell* [1997].

heterogeneity in the upper mantle. However, the surface and body waves typically employed in continental-scale tomography are not able to resolve vertical velocity gradients with a precision better than ~50 km, thus limiting their ability to accurately locate boundaries such as the LAB, which in certain regions appear to be relatively sharp (e.g., 5–10 km [*Rychert et al.*, 2005; *Chen et al.*, 2006]). In contrast, converted phases such as *P*-to-*s* (*Ps*) and *S*-to-*p* (*Sp*) are well suited for interrogating such upper mantle discontinuities (e.g., the *Moho*, LAB, 410-km and 660-km), and in recent years these phases have been widely used to image the LAB and discontinuities within the lithosphere [e.g., *Sacks et al.*, 1979; *Bostock*, 1998; *Li et al.*, 2000; *Collins et al.*, 2002; *Oreshin et al.*, 2002; *Li et al.*, 2004; *Kumar et al.*, 2005a, 2005b; *Rychert et al.*, 2005, 2007; *Vinnik et al.*, 2005; *Chen et al.*, 2006; *Mohsen et al.*, 2006; *Sodoudi et al.*, 2006a, 2006b; *Wölbern et al.*, 2006; *Hansen et al.*, 2007; *Heit et al.*, 2007; *Kumar et al.*, 2007; *Li et al.*, 2007; *Wittlinger and Farra*, 2007; *Ozacar et al.*, 2008; *Savage and Silver*, 2008; *Snyder*, 2008; *Chen*, 2009; *Ford et al.*, 2009; *Hansen et al.*, 2009; *Kawakatsu et al.*, 2009; *Rychert and Shearer*, 2009; *Rychert et al.*, 2010; *Fischer et al.*, 2010].

[4] Here we present a continental-scale investigation that employs *Ps* and *Sp* receiver functions to image upper mantle discontinuity structure beneath the contiguous United States and portions of southeast Canada and northwest Mexico. This study focuses on estimating the thickness of the high velocity seismic lid, which we will refer to as the lithosphere. Our results indicate at least one negative velocity contrast exists at mantle depths beneath most of the continental United States. In the tectonically active western U.S. and portions of the eastern U.S., the largest negative *Sp* phase correlates with surface wave constraints on the LAB. However, in the central U.S. and some eastern zones, the depth of the inferred discontinuity is much shallower than that estimated for the base of the lithosphere from surface and body wave tomography, suggesting the presence of layering within the lithosphere. In addition, the amplitude of negative *Sp* phases in the western U.S. is much larger than in the central and eastern U.S., indicating a stronger impedance contrast in the west, likely due to a weaker asthenosphere.

2. Data

[5] Searching the USGS National Earthquake Information Center (NEIC) global event catalog for events with M_W> = 5.8 and epicentral distance between 35° and 80° through the end of March 2009, we compiled waveform data from the Incorporated Research Institutions for Seismology (IRIS) Data Management Center (DMC) for 121 permanent seismic

Table 1. Network Affiliations for the Seismic Stations Used in This Study[a]

NET	Network Name	Institution/Affiliation
AZ	ANZA Regional Network	University of California, San Diego
BK	Berkeley Digital Seismic Network	University of California, Berkeley
CI	Caltech Regional Seismic Network	California Institute of Technology
CN	Canadian National Seismograph Network	Geological Survey of Canada
CT	California Transect Network	University of California, Santa Cruz
G	GEOSCOPE	Institut de Physique du Globe de Paris
IM	International Miscellaneous Stations	
IU	Global Seismograph Network (IRIS/USGS)	IRIS/USGS Albuquerque Seismological Laboratory
LB	Leo Brady Network	Sandia National Laboratory
LD	Lamont-Doherty Cooperative Seismographic Network	Lamont-Doherty Earth Observatory, Columbia University
LI	Laser Interferometer Gravitational-Wave Experiment (LIGO)	California Institute of Technology/USGS
NE	Northeastern United States Networks	Massachusetts Institute of Technology/Boston College
NM	Cooperative New Madrid Seismic Network	Saint Louis University/Memphis State
NR	NARS-Baja Seismic Network	California Institute of Technology/University of Utrecht
TS	TERRAscope	California Institute of Technology
UO	University of Oregon Regional Network	University of Oregon
US	United States National Seismic Network	USGS/IRIS
UW	Pacific Northwest Regional Seismic Network	University of Washington

[a]All data were acquired from the IRIS DMC.

stations from 18 different networks in the United States, Canada, and Mexico (Figure 1 and Table 1). To avoid contamination with *pPPP*, *pPPPP*, and *sPPPP* [*Wilson et al.*, 2006], we included only events with depths <300 km for *Sp* analysis. In addition, *S* waves at distances <55° are post-critical (i.e., vertical incidence angles are too large and no converted *Sp* phase will be produced) and at distances >75° *SKS* and *SKSp* phases will potentially interfere with the *Sp* phase [*Wilson et al.*, 2006]. Therefore, we further restricted our *Sp* analysis to events from epicentral distances of 55°–75°. Station operations times range from 1 to 20 years, starting as early as 1988, and the resulting data set contains more than 52,000 waveforms.

3. Receiver Function Methodology

[6] A key feature of the receiver function approach is to deconvolve parent component waveforms (P for *Ps* and SV for *Sp*) from daughter components (SV for *Ps* and P for *Sp*) in order to normalize variations in earthquake source-time functions and to enhance the signal of energy converted at impedance contrasts beneath a particular station. Although techniques for generating *Ps* and *Sp* receiver functions [*Langston*, 1977; *Vinnik*, 1977; *Ammon*, 1991; *Bostock*, 1998; *Farra and Vinnik*, 2000] have become relatively standard [e.g., *Oreshin et al.*, 2002; *Vinnik et al.*, 2004, 2005; *Kumar et al.*, 2005a, 2005b, 2006; *Rychert et al.*, 2005, 2007; *Yuan et al.*, 2006; *Li et al.*, 2007; *Rychert and Shearer*, 2009], there are several choices in the analysis process that can affect the resulting receiver functions. Furthermore, due to the large number of waveforms employed in this study (and even larger volumes likely to be used in the future application of our approach to data from the EarthScope Transportable Array) we have developed a semi-automated waveform analysis procedure. Therefore, we provide details on several key steps of our methodology in order to minimize ambiguity and to allow for our work to be more easily replicated.

3.1. Phase Picking

[7] Direct *P* and *S* phase arrival times were determined with an automated picking algorithm based on the short-term-average (STA) to long-term-average (LTA) moving window method of *Earle and Shearer* [1994]. For a point in time (e.g., t_i) along the envelope function of a seismogram, the ratio of the mean of the amplitudes in a short window following t_i (i.e., a "signal" window or the STA) to the mean of the amplitudes in a long window preceding t_i (i.e., a "noise" window or the LTA) was measured. The envelope was calculated by taking the absolute value of the Hilbert transform of the filtered waveform (0.5–1.5 Hz for *P* and 0.1–0.75 Hz for *S*; note that a slightly different bandpass is used in the deconvolution (section 3.4)). We used a signal window length of 5 and 10 seconds for the *P* and *S* phases, respectively, with a noise window length four times that of the signal window (Figures 2e and 2f). We calculated the signal-to-noise ratio (S2N) of the envelope function for a window of ± 25 seconds around the arrival time predicted by the 1-D reference Earth model AK135 [*Kennett et al.*, 1995] (Figures 2a and 2d). The S2N function was smoothed by convolving it with a Hanning window of the same length as the signal window (Figures 2g and 2h). Here, the peak value in this smoothed S2N function was taken as the phase arrival time, rather than the inflection point preceding the peak used by *Earle and Shearer* [1994]. In cases where the maximum S2N value falls below a value of 2, we relied on the predicted phase arrival time from AK135.

3.2. Determining P and SV Components

[8] To accurately recover the parent and daughter waveforms, the Z-N-E components were rotated into Z-R-T and then transformed into P-SV-SH using the free-surface transfer matrix [*Kennett*, 1991]

$$\begin{bmatrix} P \\ SV \\ SH \end{bmatrix} = \begin{bmatrix} \frac{(\beta^2 p^2 - 1/2)}{\alpha q_\alpha} & \frac{p\beta^2}{\alpha} & 0 \\ p\beta & \frac{(1/2 - \beta^2 p^2)}{\beta q_\beta} & 0 \\ 0 & 0 & \frac{1}{2} \end{bmatrix} \begin{bmatrix} Z \\ R \\ T \end{bmatrix} \quad (1)$$

where α and β are the near surface compressional and shear velocities, respectively, $q_\alpha = (\alpha^{-2} - p^2)^{0.5}$, $q_\beta = (\beta^{-2} - p^2)^{0.5}$,

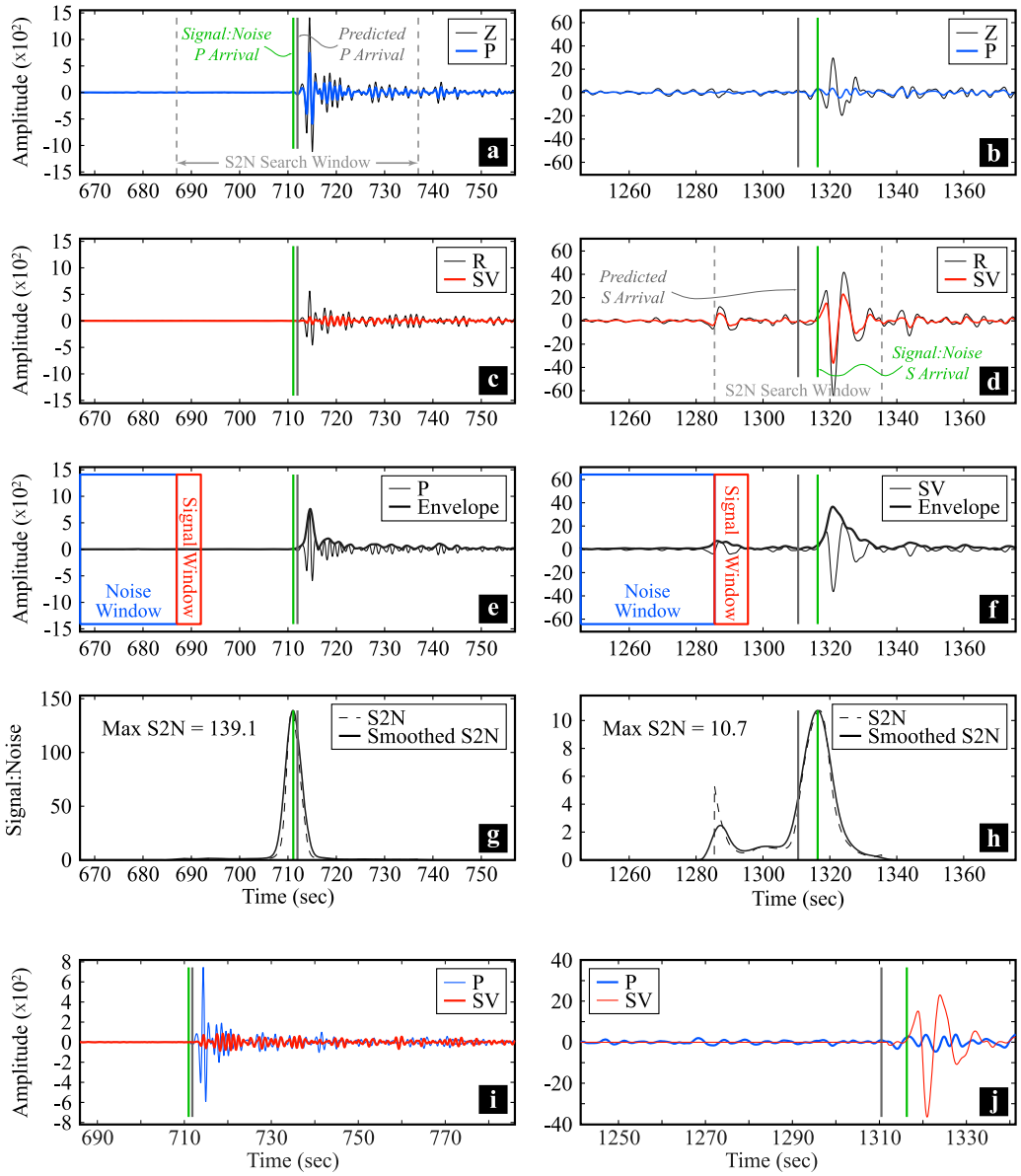

Figure 2. Example of the coordinate system rotation and phase picking routine employed in the preprocessing of waveform data: (left) Windows around the *P* arrival time and (right) windows around the *S* arrival time. For this signal:noise (S2N) analysis, waveforms for *Ps* (left) are bandpass filtered at 0.5–1.5 Hz (0.1–0.75 Hz for *Sp*, right). The Z and R components (thin black lines in Figures 2a–2d) are transformed into P and SV (thick blue and red lines in Figures 2a–2d, respectively) with the free-surface transform [*Kennett*, 1991] (see section 3.2). The large reduction in amplitude on the transformed daughter components (SV for *Ps* and P for *Sp*) relative to the Z-R components is easily observed. The vertical gray line shows the predicted phase arrival time from the 1-D reference Earth model AK135 [*Kennett et al.*, 1995]. Figures 2e and 2f display the envelope of each parent waveform and the signal and noise windows used. The window of time for which S2N is calculated is shown in Figures 2a and 2d. The resulting S2N functions are in Figures 2g and 2h, and the peak in S2N is indicated by the vertical green line, which also appears in Figures 2a–2f, 2i, and 2j. Although the predicted AK135 and calculated S2N arrival times are similar for *P*, a more accurate pick of the *S* arrival is made by the S2N analysis. The full windows used in the deconvolution are shown in Figures 2i and 2j; note the slight difference in time scale in Figures 2a–2h.

and p is the ray parameter of the direct phase. The free-surface velocities (α, β) were determined for each waveform at a particular station by finding values for V_P (between 3.5 and 7 km/sec) and V_P/V_S (between 1.6 and 2.0) that, when applied in equation (1), minimized the correlation between the P and SV components in a short window around the phase arrival. For *Ps*, we chose a window from $0.5T_P$ seconds before to T_P seconds after the *P* arrival, where T_P is the dominant *P* period.

For *Sp*, the window starts at the *S* arrival and its length equals the dominant *S* period. We stacked all cross-correlation surfaces that have a well-defined minimum correlation in V_P-V_P/V_S space for both the *P* and *S* arrivals, and defined the best free-surface velocities for a particular station as the minimum of this stack. We tested this approach with synthetic seismograms and found that our use of the free-surface transform accurately separated the P and SV components and that the free-surface V_P and V_P/V_S values retrieved from stacking cross-correlation surfaces matched the model used to generate the synthetics. We also experimented with allowing the incident phase ray parameter to vary from its initial value, but this step had a negligible effect on results with real data. Note that our method differs from other studies [e.g., *Oreshin et al.*, 2002; *Vinnik et al.*, 2004; *Kumar et al.*, 2005a, 2005b; *Li et al.*, 2007] in which the P and SV components are assumed to be orthogonal and are determined by rotating the vertical and radial waveforms until the P component amplitude at the direct *S* arrival time sample is minimized.

3.3. Deconvolution

[9] Because of the relatively small magnitude of scattered wave energy on individual waveforms (e.g., Figures 2b and 2c), we enhanced the signal of converted waves by combining all waveforms at a particular station. For *Ps*, the daughter component (SV) window included 25 s before and 75 s after the direct *P* arrival pick (Figure 2i); for *Sp*, the window was 75 s before and 25 s after the direct *S* arrival (Figure 2j). The parent components were tapered to zero with a 0.5 s cosine taper before the phase arrival pick. Waveforms were first bandpass filtered (0.03–1 Hz for *Ps* and 0.03–0.5 Hz for *Sp*) and then normalized by the maximum amplitude of the parent component and weighted according to the parent phase S2N.

[10] We retrieved a response function (i.e., our receiver function) in time (RF_{time}) by deconvolving the parent phase from the daughter component for a range of possible conversion depths (z_c). We employed a simultaneous deconvolution in the frequency domain (following *Bostock* [1998])

$$RF_{time}(z_c) = F^{-1}\left(\frac{\sum_{i=1}^{N} DC_i(\omega)PC_i^*(\omega)e^{i\omega\tau_{p_i z_c}}}{\sum_{i}^{N} PC_i(\omega)PC_i^*(\omega) + \delta}\right) \quad (2)$$

where PC_i and DC_i are the i^{th} waveforms (in the frequency-domain, ω) of the parent (P for *Ps* and SV for *Sp*) and daughter (SV for *Ps* and P for *Sp*) components, respectively; the * indicates the complex conjugate, F^{-1} is the inverse Fourier transform. To correct for the different move-out of phases with different ray parameters, a time shift (τ) was applied to each waveform to align it with a reference ray parameter (p_{ref}); we chose a p_{ref} corresponding to an epicentral distance of 60° for *Ps* and 65° for *Sp*. τ is a function of ray parameter (p_i) and conversion depth (z_c). δ is a regularization parameter (water level) and effectively acts as a low-pass filter. δ was chosen objectively such that the general cross validation function of the parent and daughter waveforms was minimized [*Golub et al.*, 1979]. In other words, the chosen water level produced the receiver function that when convolved with the parent component best-replicated the daughter component [see *Bostock*, 1998, equations 4–6]. We also calculated receiver functions with an iterative time-domain deconvolution [*Ligorria and Ammon*, 1999] to determine if artifacts from spectral division in the frequency-domain deconvolution (i.e., side-lobes) contaminate the phases observed on the receiver functions presented in section 4. The results of the two methods in general agree, and side-lobes and similar artifacts have negligible impact on the phases interpreted in this study.

[11] The critical ray parameter for a converted phase changes with discontinuity depth such that *Sp* conversions at mantle depths are sometimes not predicted for the lower end of our epicentral distance range in the assumed mantle velocity models. Therefore, only waves with pre-critical ray parameters for a particular discontinuity depth were included in the deconvolution when calculating the RF_{time} for that particular depth. Pre-critical *Ps* conversions are predicted at all depths within the epicentral distance range investigated here (35°–80°).

3.4. Migration

[12] The receiver functions in time from equation (2) were mapped to depth by extracting amplitudes from each $RF_{time}(z_c)$ according to the predicted delay time (*Ps*-*P* or *Sp*-*S*) versus depth function for a particular upper mantle velocity model for the reference ray. We calculated and migrated receiver functions assuming two different velocity models. Crustal parameters in both models were either calculated by H-*k* stacking of *Ps* waveforms [*Zhu and Kanamori*, 2000] or taken from Crust2.0 [*Bassin et al.*, 2000] when the *Ps* receiver functions displayed too much complexity at crustal depths to permit simple interpretation of H-*k* stacks (Table 2). The first mantle model is the 1-D reference Earth model AK135 [*Kennett et al.*, 1995]. The second is a three-dimensionally varying model, in which 1-D velocity models for each station were constructed using mantle V_P from *Burdick et al.* [2008] and mantle V_S from *Yuan and Romanowicz* [2010]. The absolute V_P and V_S profiles for each station were azimuthal averages of the respective model at a distance of 125 km from station. This distance approximates *Sp* conversion point distances from the station for a discontinuity at 100 km depth.

[13] The mantle V_S model is the isotropic component of the UC-Berkeley 3-D tomographic shear wave velocity structure of the North American continent [*Yuan and Romanowicz*, 2010]. In the framework of normal mode asymptotic coupling theory [*Li and Romanowicz*, 1995], which includes finite frequency kernels, we simultaneously inverted long period surface waveforms for isotropic S-velocity structure and a parameter that describes V_{SH} versus V_{SV} anisotropy (ξ) [*Marone et al.*, 2007]. The surface-wave dataset consisted of over 150,000 3-component fundamental and higher mode waveforms from permanent and temporary broadband seismic stations across the continent, including the USArray Transportable Array and Permanent Backbone stations and the Canadian National Seismograph Network, which greatly improve path and azimuth coverage. The model was constructed starting from a new global 1D reference Earth model that is based on a combination of seismic and mineral physics data [*Cammarano and Romanowicz*, 2007] and is smooth

Table 2. Summary of Observed Receiver Function Parameters[a]

				Crustal Model				Receiver Function Interpretations				
NET	STA	#Ps	#Sp	Source	Moho	Vp	Vp/Vs	M_{3D} (M_{1D})	ε_{M3D} (ε_{M1D})	N_{3D} (N_{1D})	ε_{N3D}(ε_{N1D})	LAB?
BK	CMB	724	340	Crust2.0	38	6.31	1.78	41 (41)	2 (1)	78 (76)	8 (9)	LAB
BK	JRSC	188	106	H-k Stack	33	6.39	1.59	32 (32)	3 (3)	-	-	-
BK	ORV	238	117	H-k Stack	34	6.48	1.85	35 (35)	4 (4)	78 (77)	8 (9)	LAB
BK	PKD	197	101	H-k Stack	28	6.18	1.81	30 (29)	2 (2)	79 (76)	18 (18)	LAB
BK	WDC	274	144	Crust2.0	37	6.56	1.77	26 (27)	2 (2)	70 (68)	15 (16)	LAB
BK	YBH	108	53	Crust2.0	34	6.56	1.77	37 (37)	8 (7)	59 (58)	8 (8)	LAB
CI	CWC	482	273	H-k Stack	30	6.27	1.8	32 (30)	32 (30)	-	-	-
CI	DGR	626	326	H-k Stack	33	6.23	1.78	34 (34)	1 (1)	67 (65)	9 (9)	LAB
CI	GSC	607	313	H-k Stack	23	6.25	1.96	26 (26)	2 (2)	61 (59)	6 (6)	LAB
CI	PAS	869	500	H-k Stack	27	6.26	1.76	28 (28)	3 (3)	70 (66)	8 (8)	LAB
CI	RPV	436	236	H-k Stack	29	6.28	1.6	30 (30)	2 (2)	65 (63)	8 (7)	LAB
CI	SVD	336	173	H-k Stack	31	6.22	1.96	31 (31)	2 (2)	79 (75)	18 (16)	LAB
CI	TOV	411	230	H-k Stack	23	6.25	1.91	36 (35)	2 (2)	75 (72)	24 (23)	LAB
CI	USC	243	227	Crust2.0	27	6.26	1.78	-	-	58 (55)	13 (12)	LAB
CI	**VTV**	**369**	**187**	**H-k Stack**	**25**	**6.24**	**1.92**	**25 (25)**	**2 (2)**	**68 (66)**	**10 (10)**	**LAB**
CN	SADO	187	120	H-k Stack	38	6.49	1.77	40 (40)	2 (2)	90 (90)	21 (19)	MLD
CN	**ULM**	**205**	**85**	**H-k Stack**	**34**	**6.42**	**1.73**	**36 (36)**	**2 (2)**	**101 (96)**	**14 (14)**	**MLD**
CT	FERN	45	24	Crust2.0	29	6.38	1.79	24 (25)	16 (14)	66 (63)	8 (7)	LAB
CT	SAVY	10	8	Crust2.0	31	6.35	1.79	25 (25)	2 (2)	-	-	-
G	SCZ	735	419	H-k Stack	24	6.32	1.77	25 (24)	4 (3)	70 (66)	15 (16)	LAB
IM	NV31	176	94	H-k Stack	36	6.28	1.74	37 (36)	2 (2)	102 (100)	10 (9)	LAB
IM	PD31	340	143	Crust2.0	45	6.18	1.76	36 (36)	1 (1)	-	-	-
IM	TX31	272	148	H-k Stack	36	6.34	1.8	37 (37)	2 (2)	83 (82)	19 (19)	LAB
IM	TX32	245	138	H-k Stack	36	6.34	1.81	36 (36)	1 (1)	80 (79)	17 (17)	LAB
IU	CCM	373	256	H-k Stack	45	6.5	1.79	46 (46)	2 (1)	88 (86)	19 (13)	???
IU	DWPF	312	201	H-k Stack	35	6.24	1.91	36 (36)	2 (2)	-	-	-
IU	HKT	340	275	H-k Stack	34	5.73	1.61	36 (35)	2 (2)	76 (73)	9 (9)	LAB
IU	**HRV**	**635**	**421**	**H-k Stack**	**31**	**6.4**	**1.66**	**33 (33)**	**2 (2)**	**111 (106)**	**7 (7)**	**LAB**
IU	SSPA	242	140	Crust2.0	39	6.32	1.76	-	-	109 (108)	38 (12)	???
IU	TUC	500	241	H-k Stack	31	6.22	1.68	33 (33)	3 (3)	80 (79)	7 (7)	LAB
IU	WCI	289	177	Crust2.0	41	6.47	1.77	52 (52)	5 (4)	97 (93)	7 (7)	MLD
IU	WVT	298	203	H-k Stack	36	6.46	1.99	38 (38)	1 (1)	113 (110)	7 (6)	MLD
LB	BMN	406	178	H-k Stack	29	6.28	1.77	30 (30)	2 (2)	51 (51)	32 (30)	LAB
LB	DAC	172	89	H-k Stack	32	6.28	1.75	33 (33)	4 (4)	-	-	-
LB	MVU	62	39	H-k Stack	38	6.23	1.79	42 (41)	2 (3)	-	-	-
LB	TPH	402	190	H-k Stack	35	6.28	1.77	36 (36)	2 (2)	83 (81)	8 (7)	LAB
LD	ACCN	311	204	H-k Stack	44	6.44	1.79	45 (45)	2 (2)	73 (73)	12 (10)	???
LD	BRNJ	246	153	H-k Stack	40	6.14	1.79	40 (41)	3 (3)	89 (87)	8 (8)	LAB
LD	LOZ	26	22	H-k Stack	41	6.42	1.86	42 (43)	3 (4)	-	-	-
LD	MVL	263	161	Crust2.0	33	6.31	1.79	45 (44)	6 (6)	75 (72)	16 (15)	LAB
LD	PAL	456	298	H-k Stack	40	6.17	1.67	42 (42)	3 (3)	79 (77)	10 (9)	LAB
LD	PTN	104	58	H-k Stack	39	6.42	1.81	38 (37)	2 (3)	69 (68)	11 (11)	MLD
LD	**SDMD**	**253**	**159**	**H-k Stack**	**30**	**6.3**	**1.71**	**32 (32)**	**3 (3)**	**105 (101)**	**9 (9)**	**???**
LI	LTH	285	138	H-k Stack	33	6.55	1.87	33 (33)	1 (1)	76 (75)	14 (14)	LAB
NE	FFD	86	64	Crust2.0	37	6.42	1.76	29 (29)	2 (2)	-	-	-
NE	HNH	19	57	Crust2.0	34	6.45	1.78	32 (30)	7 (5)	-	-	-
NE	PQI	87	70	H-k Stack	33	6.42	1.79	34 (34)	3 (2)	-	-	-
NE	WES	73	62	H-k Stack	30	6.36	1.73	32 (32)	2 (2)	-	-	-
NE	WVL	78	45	H-k Stack	35	6.42	1.74	35 (36)	2 (3)	98 (94)	12 (11)	LAB
NE	YLE	73	51	H-k Stack	30	6.25	1.74	32 (32)	3 (2)	-	-	-
NM	BLO	398	234	Crust2.0	41	6.48	1.77	52 (51)	2 (2)	111 (106)	14 (13)	MLD
NM	**FVM**	**210**	**125**	**Crust2.0**	**42**	**6.46**	**1.78**	**46 (45)**	**3 (3)**	**101 (99)**	**11 (10)**	**???**
NM	MPH	188	215	Crust2.0	38	6.31	1.78	38 (38)	2 (2)	-	-	-
NM	PLAL	211	148	Crust2.0	36	6.51	1.77	45 (44)	8 (7)	83 (81)	8 (7)	MLD
NM	SIUC	331	206	Crust2.0	41	6.44	1.77	49 (49)	3 (2)	75 (73)	8 (8)	???
NM	SLM	416	230	H-k Stack	44	6.45	1.93	45 (44)	2 (3)	77 (76)	13 (13)	???
NM	UALR	200	165	H-k Stack	29	6.25	1.93	30 (30)	3 (3)	104 (100)	12 (15)	???
NM	UTMT	209	180	H-k Stack	21	6.44	2	23 (23)	1 (1)	76 (72)	7 (6)	???
NR	NE70	97	55	Crust2.0	30	6.26	1.78	-	-	52 (50)	11 (9)	LAB
NR	NE71	169	73	H-k Stack	33	6.26	1.82	34 (34)	2 (2)	67 (66)	7 (7)	LAB
TS	PFO	356	211	H-k Stack	29	6.2	1.72	29 (29)	2 (2)	77 (73)	12 (14)	LAB
UO	PIN	254	129	Crust2.0	37	6.42	1.77	45 (42)	11 (8)	66 (65)	6 (6)	LAB
US	AAM	215	114	H-k Stack	41	6.49	1.91	43 (41)	6 (7)	90 (86)	11 (9)	MLD
US	ACSO	251	159	H-k Stack	43	6.25	1.86	44 (44)	16 (15)	-	-	-
US	BINY	309	209	Crust2.0	36	6.3	1.76	43 (43)	11 (10)	122 (116)	44 (43)	???
US	BLA	266	168	Crust2.0	37	6.43	1.76	35 (36)	2 (2)	69 (68)	12 (9)	MLD
US	CBKS	330	173	H-k Stack	47	6.45	1.77	48 (48)	1 (1)	69 (68)	8 (8)	???
US	CBM	6		H-k Stack	39	6.42	1.78	41 (41)	3 (3)	-	-	-
US	CBN	187	120	Crust2.0	32	6.37	1.78	-	-	90 (87)	20 (22)	???
US	CEH	25	15	H-k Stack	34	6.54	1.81	34 (34)	2 (2)	99 (95)	11 (10)	MLD

Table 2. (continued)

				Crustal Model				Receiver Function Interpretations				
NET	STA	#Ps	#Sp	Source	Moho	Vp	Vp/Vs	M_{3D} (M_{1D})	ε_{M3D} (ε_{M1D})	N_{3D} (N_{1D})	ε_{N3D}(ε_{N1D})	LAB?
US	ELK	397	145	H-k Stack	31	6.28	1.74	32 (32)	2 (2)	56 (54)	6 (7)	LAB
US	EYMN	212	75	H-k Stack	41	6.47	1.79	44 (44)	2 (2)	94 (89)	10 (10)	MLD
US	GOGA	151	98	H-k Stack	31	6.53	2	41 (32)	3 (2)	101 (90)	5 (5)	LAB
US	GWDE	35	29	Crust2.0	29	5.95	1.8	38 (38)	3 (3)	-	-	-
US	ISA	38	22	H-k Stack	31	6.24	1.92	32 (32)	2 (1)	62 (61)	12 (11)	LAB
US	ISCO	386	162	H-k Stack	25	6.19	1.98	45 (43)	4 (3)	79 (76)	21 (20)	LAB
US	JCT	212	151	H-k Stack	44	6.35	1.86	45 (44)	2 (2)	94 (94)	9 (12)	LAB
US	JFWS	194	97	H-k Stack	35	6.53	1.98	37 (36)	3 (3)	59 (58)	12 (11)	MLD
US	LBNH	297	189	Crust2.0	39	6.42	1.75	40 (40)	3 (3)	99 (93)	27 (35)	LAB
US	LKWY	265	186	H-k Stack	30	6.2	1.61	30 (30)	2 (2)	90 (87)	7 (6)	???
US	LRAL	189	127	Crust2.0	32	6.46	1.78	49 (48)	2 (2)	91 (91)	21 (19)	MLD
US	LSCT	26	53	H-k Stack	25	6.37	1.9	24 (24)	3 (3)	-	-	-
US	LTX	202	125	H-k Stack	36	6.34	1.8	37 (37)	2 (2)	81 (79)	12 (22)	LAB
US	MCWV	280	178	Crust2.0	44	6.22	1.76	47 (45)	3 (2)	91 (87)	11 (12)	MLD
US	MIAR	264	175	H-k Stack	47	6.29	1.77	49 (49)	2 (2)	-	-	-
US	MNV	256	67	H-k Stack	36	6.28	1.73	37 (37)	2 (1)	80 (78)	10 (12)	LAB
US	MYNC	54	42	Crust2.0	37	6.45	1.77	55 (54)	2 (2)	-	-	-
US	NCB	319	204	H-k Stack	39	6.42	1.91	40 (40)	2 (2)	109 (106)	19 (19)	???
US	NHSC	148	116	Crust2.0	30	6.2	1.79	36 (36)	5 (5)	57 (55)	6 (6)	???
US	SAO	183	100	Crust2.0	28	6.33	1.79	34 (32)	28 (21)	79 (75)	13 (12)	LAB
US	WMOK	167	119	H-k Stack	31	6.39	1.53	30 (30)	3 (3)	84 (81)	7 (8)	???
UW	GNW	191	151	Crust2.0	38	6.58	1.77	-	-	104 (104)	6 (6)	LAB
UW	LTY	195	104	Crust2.0	40	6.52	1.76	-	-	104 (104)	7 (6)	LAB

[a]For each station, the number of waveforms used in the deconvolution and the crustal model used in the migration are given. The depth picks of the most prominent positive *Ps* (M) and negative *Sp* (N) phase from the receiver functions are presented for both the 3-D and 1-D (in parentheses) migration models, along with their errors (ε). Based on the 3-D V_S model used here, we interpret the negative *Sp* phase as the lithosphere-asthenosphere boundary (LAB), a mid-lithospheric discontinuity (MLD), or as a discontinuity of ambiguous origin (???). See the beginning of section 4 for an explanation of the basis for these interpretations. Individual stations shown in Figures 4–8 are in bold (VTV, ULM, HRV, FVM, and SDMD).

at 220 km. A crustal correction approach that accounts for non-linearities was employed [*Lekić et al.*, 2010].

[14] The choice of velocity model, in particular the V_P-V_S ratio, has an impact on the depth to which the receiver function phases migrate, but we found very little difference in the receiver functions migrated with AK135 and those from the 3-D model. Although we present depths from both models in Table 2, for simplicity, all receiver functions shown in this paper were migrated with the 1-D station profiles extracted from the 3-D mantle velocity model.

3.5. Error Estimation

[15] Errors were estimated for individual receiver functions by bootstrapping. For both *Ps* and *Sp* at each station, 20% of the waveforms were replaced with another random 20% of the waveforms, and the receiver functions were recalculated. This process was repeated 100 times and both the mean and standard deviation (σ) of the resulting set of receiver functions were calculated. We consider the well-resolved portions of the receiver functions to be those still significant at 2σ from the mean receiver function (i.e., positive amplitudes below the mean-2σ and negative amplitudes above the mean+2σ). Errors in depth (amplitude) estimates were calculated from the maximum distance in depth (amplitude) from the pick to the mean ± 2σ (Figure 3). Although the receiver functions presented here were generated by stacking all available data, we also tried culling the data by both S2N and by the misfit between the direct phase arrival time predicted by AK135 and that calculated from the S2N analysis. When excluding *Ps* and *Sp* waveforms with S2N less than 4 and 2, respectively, as well as phase arrival time discrepancies of more than 15 s, we

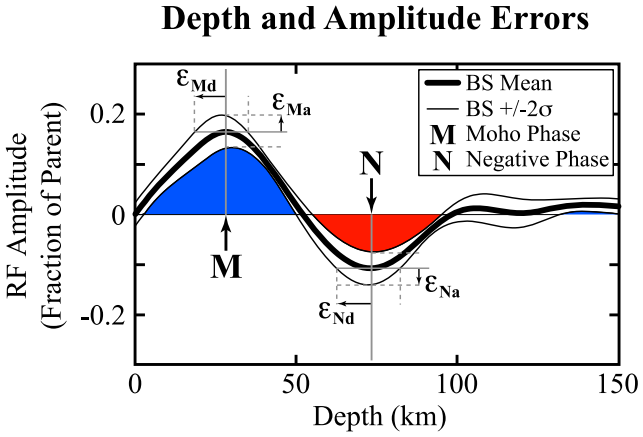

Figure 3. Illustration of receiver function parameter error estimates. The thick black line is the mean receiver function from the bootstrap testing, and the thin black lines on either side of the mean are the bootstrap ± 2 standard deviations (2σ). For the Moho (M) phase pick, the error in depth (ε_{Md}) is taken as the maximum distance from the pick on the mean receiver function to the $+2\sigma$ line; for the negative phase pick (N), the -2σ line is used to measure the error (ε_{Nd}). Error in amplitude (ε_{Ma} or ε_{Na}) is simply the 2σ value at the depth of the pick. Although we illustrate these error estimates on the same receiver function here, the values found in Table 2 have been calculated from either *Ps* for M or *Sp* for N.

found no appreciable difference between the culled receiver functions and those calculated using all available data.

4. Results and Observations

[16] Of the 121 stations in our data set (Figure 1), 93 were found to have interpretable *Ps* (87) and/or *Sp* (73) receiver functions (Table 2 and auxiliary material Figure S1 and Table S1), and we present these in several formats.[1] First, five receiver function examples at individual stations from different tectonic regions are given to illustrate the phases that we interpret (Figures 4–8), and results for all stations are summarized in Table 2. Second, to display the receiver function interpretations as a whole, the depths and amplitudes of the most prominent "negative" phase observed on the *Sp* receiver functions are plotted in map view (Figure 9). The depths of the first and largest positive phase in the *Ps* receiver functions (the phase from the Moho) are shown in auxiliary material Figure S2. As in most receiver function studies, we have reversed the amplitude of the *Sp* receiver functions to allow for a direct comparison with the *Ps* receiver functions; with this convention, a negative phase corresponds to a drop in velocity with depth. Lastly, four cross-sections through the study region demonstrate the variations of both the Moho and negative *Sp* phase depths with respect to the *Sp* receiver functions (Figure 10).

4.1. Rationale for Discontinuity Depth Estimates From Receiver Functions

[17] Moho depths were inferred from the first major positive phase in the *Ps* receiver functions at reasonable depths (i.e., 20–60 km), but this phase is typically present in the *Sp* receiver functions as well (e.g., Figures 4a–4d). Crustal multiples from the *P* phase conversion at the Moho (e.g., *Ppps*, *Psps*, *Ppss*) typically migrate to depths of 100–200 km (i.e., within the predicted LAB depth range for much of the central and eastern U.S.); crustal reverberations migrate to greater depth at larger epicentral distances and are often prominent and easily distinguishable from direct conversions, which do not move out (e.g., Figure 4b). These reverberations can mask other direct phases (e.g., the LAB), and to avoid this interference, mantle discontinuity depths were picked from the largest negative phase in the *Sp* receiver function below the Moho phase. In making these depth estimates, we assessed both the individual receiver functions (Figures 4a–8a and 4c–8c) and phase consistency across receiver functions binned by epicentral distance (Figures 4b–8b and Figures 4d–8d). When multiple negative phases exist in the *Sp* receiver functions, we selected the phase with the largest (most negative) amplitude. However, this choice of a single depth for inclusion in Table 2 obviously does not preclude the interpretation of other phases as indicating significant upper mantle structure.

[18] To guide our interpretation of the negative phases picked on the *Sp* receiver functions as either the LAB or a mid-lithospheric discontinuity (MLD), we compared the depth of these phases with absolute V_S in the 3-D shear velocity model used in the migration [*Yuan and Romanowicz*, 2010]. We estimated the most likely LAB depth range from the V_S model to be from the minimum V_S below the Moho up to the next local peak in V_S (i.e., the transition from the most prominent low velocity zone, LVZ, to the overriding high velocity lid). In the western U.S. (e.g., station VTV, Figure 4) and within the cratonic core of the continent (e.g., station ULM, Figure 5) interpretation of the potential LAB depth range from the V_S model is straightforward. However, over a significant fraction of the central U.S. and the Phanerozoic eastern U.S., the absolute V_S profiles are fast with respect to the reference Earth model AK135 and contain two local minima, one typically near 100 km depth and a second near 200–250 km depth (Figures 6e–8e). In these circumstances, potential LAB depth ranges were defined only when the true V_S minimum below the Moho is more than 0.5% slower relative to any other local minimum. For example, the two V_S minima at station HRV are 4.5633 km/s (100 km) and 4.5979 km/s (220 km), yielding a difference of 0.7570% (Figure 6e). Where this criterion is not met, no potential LAB depth range was defined and the interpretation of the negative *Sp* phase was designated as "ambiguous". This situation occurs, for example, at station FVM where the two V_S minima have a difference of only 0.1166% (Figure 7e) and at station SDMD where the difference in V_S between the two minima is 0.3467% (Figure 8e).

[19] Although the depth of the maximum negative velocity gradient has also been used to define the LAB (see *Eaton et al.* [2009] for a review of seismological definitions of the LAB), we found that, in the V_S model used here, the depth of the most negative dV_S/dz value in our estimated LAB depth range is often not the maximum negative dV_S/dz (the absolute minimum in dV_S/dz). However, for comparison, we illustrate both the estimated LAB depth range (gray shaded regions in Figures 4–6) and all local minima in dV_S/dz (gray circles in Figures 4–8; the larger circle denotes the depth of the most negative dV_S/dz).

4.2. Selected Receiver Function Examples

4.2.1. VTV (CI): San Andreas Fault (Southern California, U.S.)

[20] Station VTV is located on the northern side of the southern San Andreas Fault near the southwestern edge of the Basin and Range (Figure 1) where upper mantle velocities are considerably slower than beneath the central and eastern U.S. [e.g., *van der Lee and Nolet*, 1997; *Grand*, 2002; *Marone et al.*, 2007; *Burdick et al.*, 2008, *Nettles and Dziewonski*, 2008; *Yuan and Romanowicz*, 2010]. Crustal thickness estimates from H-*k* stacking and from the migrated *Ps* receiver functions (Figure 4a) are 25 km and 25 ± 2 km, respectively (Table 2), and are somewhat smaller than those from Crust2.0 [*Bassin et al.*, 2000] (28 km) and *Chulick and Mooney* [2002] (~30 km).

[21] The *Sp* receiver function displays a single large positive Moho phase (at a depth similar to the *Ps* Moho) and a single large negative phase at 68 ± 10 km (Figure 4c). The depth of the negative *Sp* phase (horizontal magenta line) falls within the transition from the LVZ to the shallow higher velocity lid (gray region in Figure 4). Therefore, this phase was interpreted as the LAB. The inferred depth of the LAB at VTV is comparable to values found in the *Sp* receiver function study of *Li et al.* [2007]. The amplitude of the negative *Sp* phase at VTV, as well as at other stations in the western U.S. in general, is larger than at most stations in the central

[1] Auxiliary materials are available in the HTML. doi:10.1029/2009jb006914.

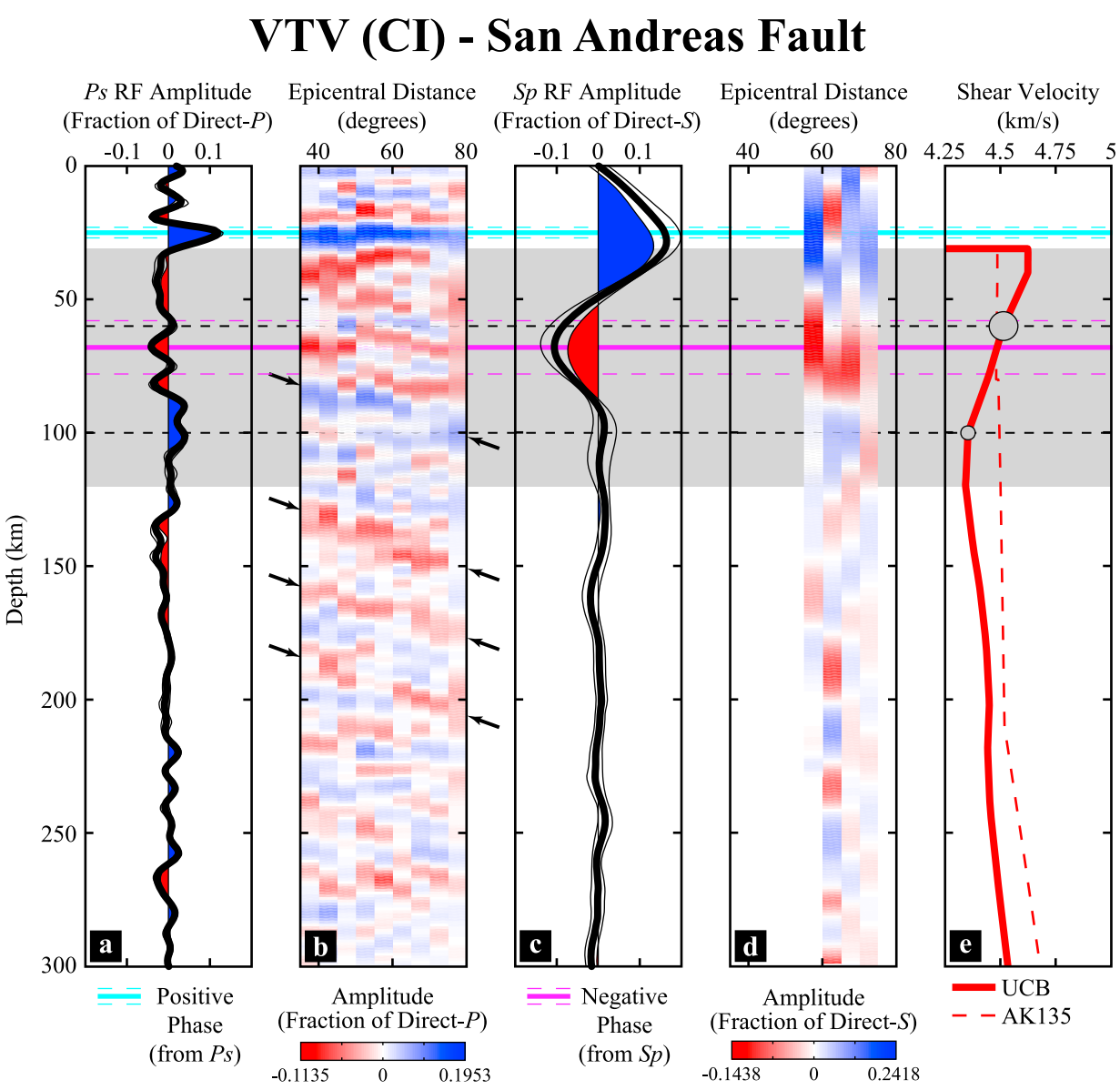

Figure 4. *Ps* and *Sp* receiver functions and V_S at station VTV. As in Figure 3, the mean single receiver functions (Figures 4a and 4c) from the bootstrap testing are shown as thick black lines and ± 2σ is given by the thin black lines. The *Ps* and *Sp* receiver functions binned by distance are in Figures 4b and 4d, respectively, and are not bootstrapped. Blue indicates positive amplitude (a velocity increase with increasing depth) and red indicates negative. In Figures 4a and 4c, the portions colored red and blue represent the minimum absolute values of amplitude, accounting for the 2σ uncertainties. The Moho phase (the large positive phase at 25 km depth) is picked on the *Ps* receiver function and highlighted with the horizontal cyan line across each plot, and the most prominent negative phase following the Moho is picked on the *Sp* receiver function and marked with the magenta line at 68 km depth. 2σ errors for both the Moho and negative *Sp* phase are given by the dashed cyan and magenta lines, respectively. Clear crustal reverberations are marked in Figure 4b with black arrows. The mantle shear velocity profile at VTV extracted from the 3-D model [*Yuan and Romanowicz*, 2010] is shown with the thick red line in Figure 4e; the dashed red line shows AK135 [*Kennett et al.*, 1995] for reference. The gray shaded region shows the depth range whose lower boundary is the depth of the minimum V_S value below the Moho and whose upper boundary is the next peak in V_S (i.e., where dV_S/dz becomes negative). We consider this gray region the most likely location for the LAB based on the 3-D V_S model. If the most prominent negative *Sp* phase falls within this region, as is the case here, we interpret the phase to represent a conversion at the LAB (Table 2). Gray circles mark points in the V_S profile where a local minimum (negative trough) in the gradient of V_S exists, with the larger circle being the most negative minimum (most negative dV_S/dz); thin dashed black lines extend from these points. VTV is representative of most stations in the western U.S. in that the negative *Sp* phase has a larger amplitude than is common in the central and eastern U.S.

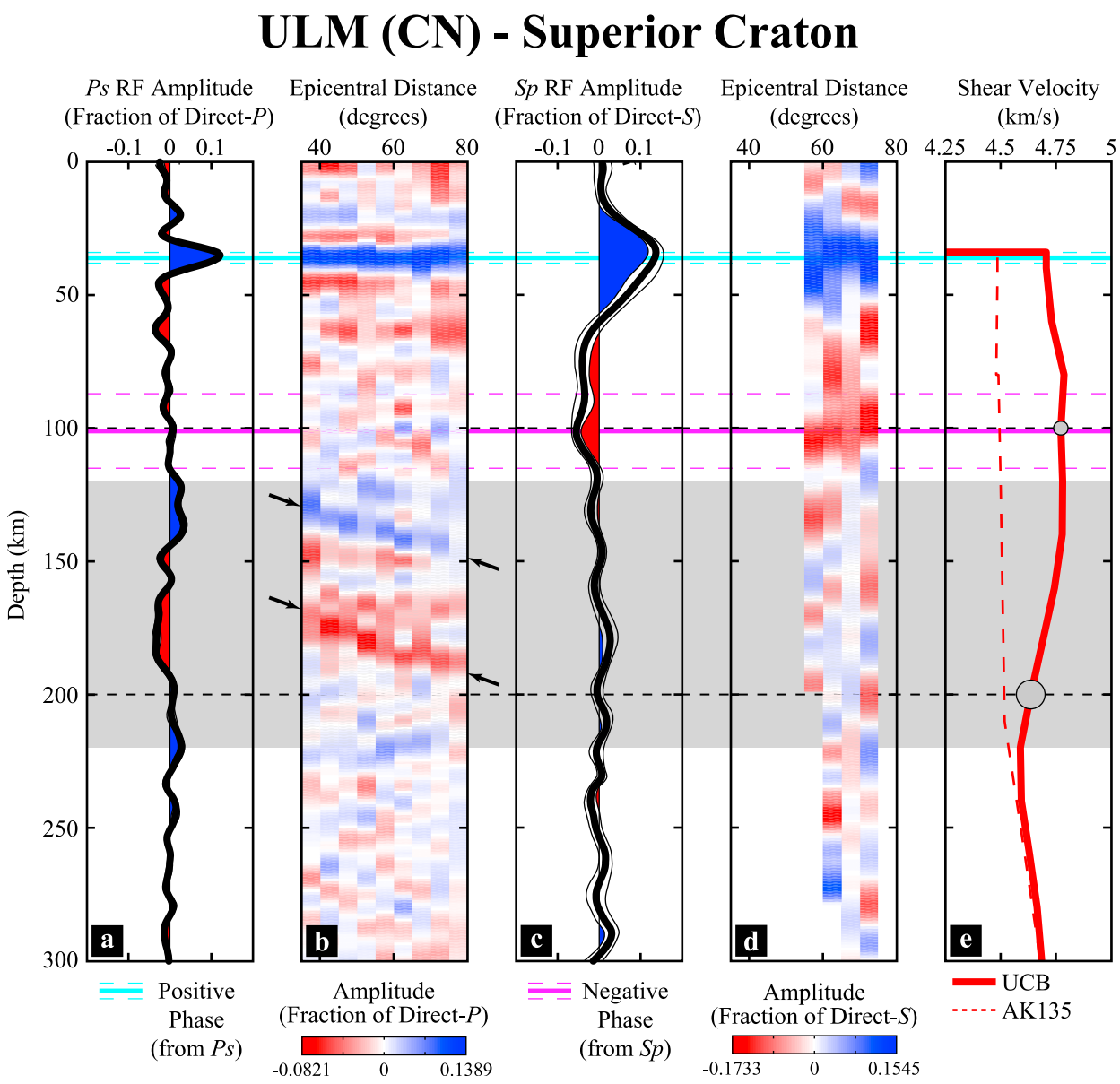

Figure 5. *Ps* and *Sp* receiver functions and V_S at station ULM. In contrast to the previous example (VTV, Figure 4), the negative *Sp* phase is shallower than the likely LAB range (gray area), and so we interpret it as the result of a mid-lithospheric discontinuity (MLD). See the caption of Figure 4 for a full explanation.

and eastern U.S. The *Ps* receiver function does contain a negative phase at a similar depth as the *Sp* "LAB" (Figures 4a and 4c), but this phase cannot be as unambiguously attributed to a direct phase given the proximity of crustal reverberations (Figure 4b).

4.2.2. ULM (CN): Superior Craton (Manitoba, Canada)

[22] Station ULM is located within the Archean Superior craton (Figure 1) where seismic studies [e.g., *van der Lee and Nolet*, 1997; *Grand*, 2002; *Godey et al.*, 2004; *Ritsema et al.*, 2004; *Darbyshire et al.*, 2007; *Marone et al.*, 2007; *Burdick et al.*, 2008; *Yuan and Romanowicz*, 2010] indicate high velocities extend to nearly 250 km depth (i.e., cratonic North American lithosphere). The Moho phase is relatively sharp in both the *Ps* and *Sp* receiver functions (Figures 5a and 5c), and clear crustal reverberations can be seen in *Ps* from 125–175 km (Figure 5b). Crustal thickness estimates from H-*k* stacking and from the migrated *Ps* receiver functions (Figure 5a) are 34 km and 36 ± 2 km, respectively (Table 2); these values are in good agreement with those from *Chulick and Mooney* [2002] (~35 km) and Crust2.0 [*Bassin et al.*, 2000] (39 km).

[23] The *Sp* receiver function contains a broad region of negative energy with its maximum amplitude at a depth of 101 ± 14 km. In this example, the high velocity lithosphere is particularly well-defined in the V_S model, with the maximum negative dV_S/dz occurring at depths close to the minimum V_S (200–220 km, Figure 5e). Because the negative *Sp* phase lies above the potential LAB depth range (gray region in Figure 5) we interpreted this phase as a discontinuity within the lithosphere (i.e., a MLD). No significant *Sp* energy is found within the likely LAB depth range, suggesting that any velocity

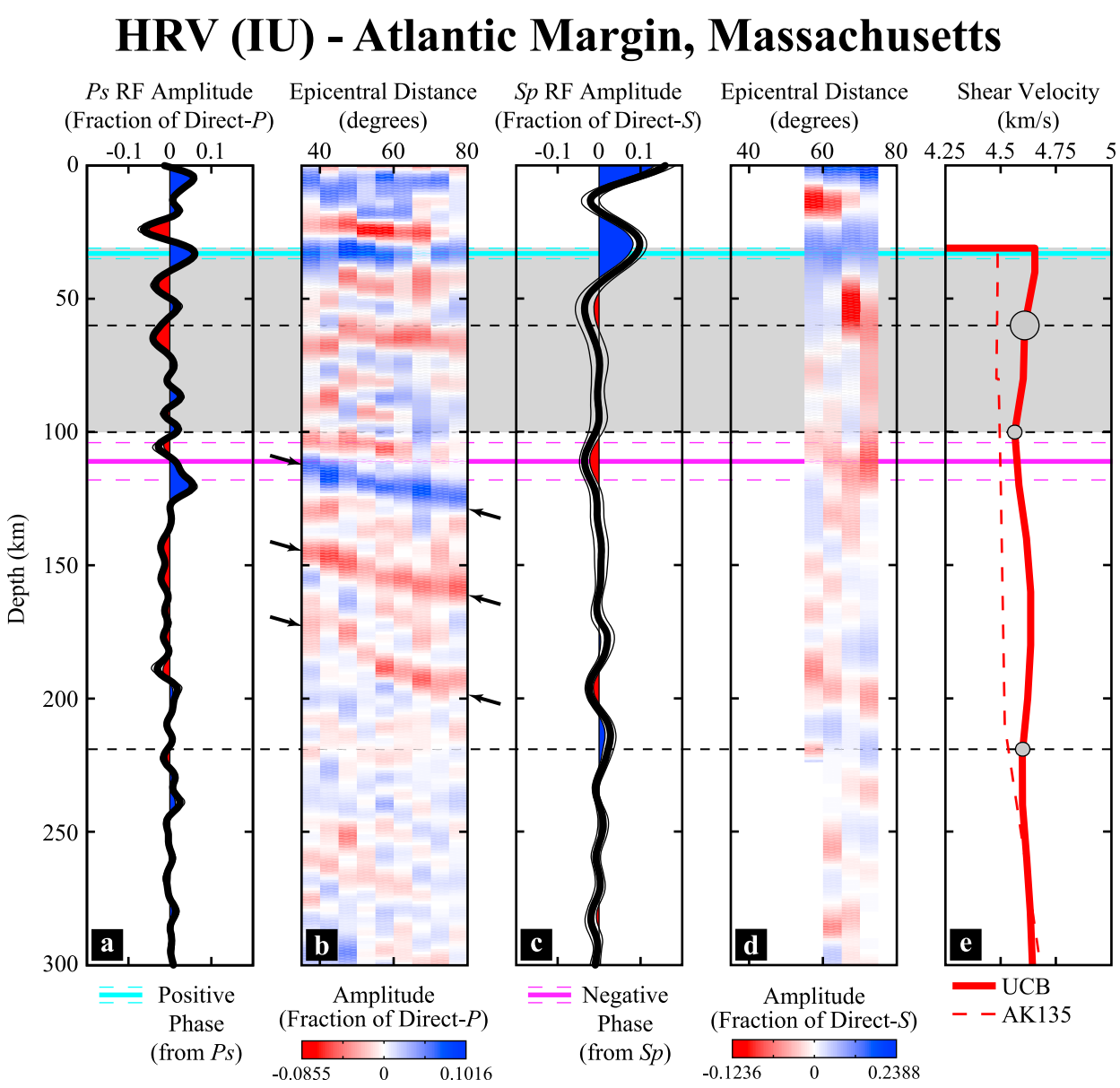

Figure 6. *Ps* and *Sp* receiver functions and V_S at station HRV. In this case, the negative *Sp* phase picked (111 ± 7 km) is located slightly deeper than the minimum V_S (100 km), and we interpret the phase to be caused by the LAB. See the caption of Figure 4 for a full explanation.

gradient at the base of the lithosphere is too gradual to produce significant converted phases. The *Ps* receiver functions binned by epicentral distance do contain negative energy at depths of 150–175 km, but because of a negative Moho reverberation at this depth interval, these signals are difficult to interpret.

4.2.3. HRV (IU): Passive Atlantic Continental Margin (Massachusetts, U.S.)

[24] HRV is located in eastern Massachusetts along the passive Atlantic margin of North America and just to the east of a pronounced decrease in the thickness of the high velocity lid (from ~200 km to ~90 km) as imaged by surface-wave tomography [*van der Lee*, 2002; *Li et al.*, 2003]. At HRV, H-*k* stacking yields a crustal thickness of 31 km, and the peak of the Moho *Ps* phase migrated to a depth of 33 ± 2 km. These estimates of crustal thickness are consistent with previous analysis of *Ps* phases at this station [*Li et al.*, 2002; *Ramesh et al.*, 2002; *Rychert et al.*, 2005, 2007], as well as with those from Crust2.0 [*Bassin et al.*, 2000] (34 km) and *Chulick and Mooney* [2002] (~35 km).

[25] The largest negative *Sp* phase at HRV migrates to a depth of 111 ± 7 km (Figure 6c). In the V_S model, the minimum near 100 km is sufficiently small relative to the minimum near 220 km (a difference of 0.787%) that a potential LAB depth range is definable. The negative *Sp* phase falls slightly below the V_S minimum, but close enough that it was interpreted as the LAB. *Rychert et al.* [2007] also observed a similar negative *Sp* phase at HRV, but the LAB depth inferred from *Sp* in this earlier work (~90 km for a V_P/V_S of 1.8 and 96–99 km for a V_P/V_S of 1.7) is shallower than that found here (111 ± 7 km for an average V_P/V_S of 1.75). Although the receiver function methodology used here is nearly identical to

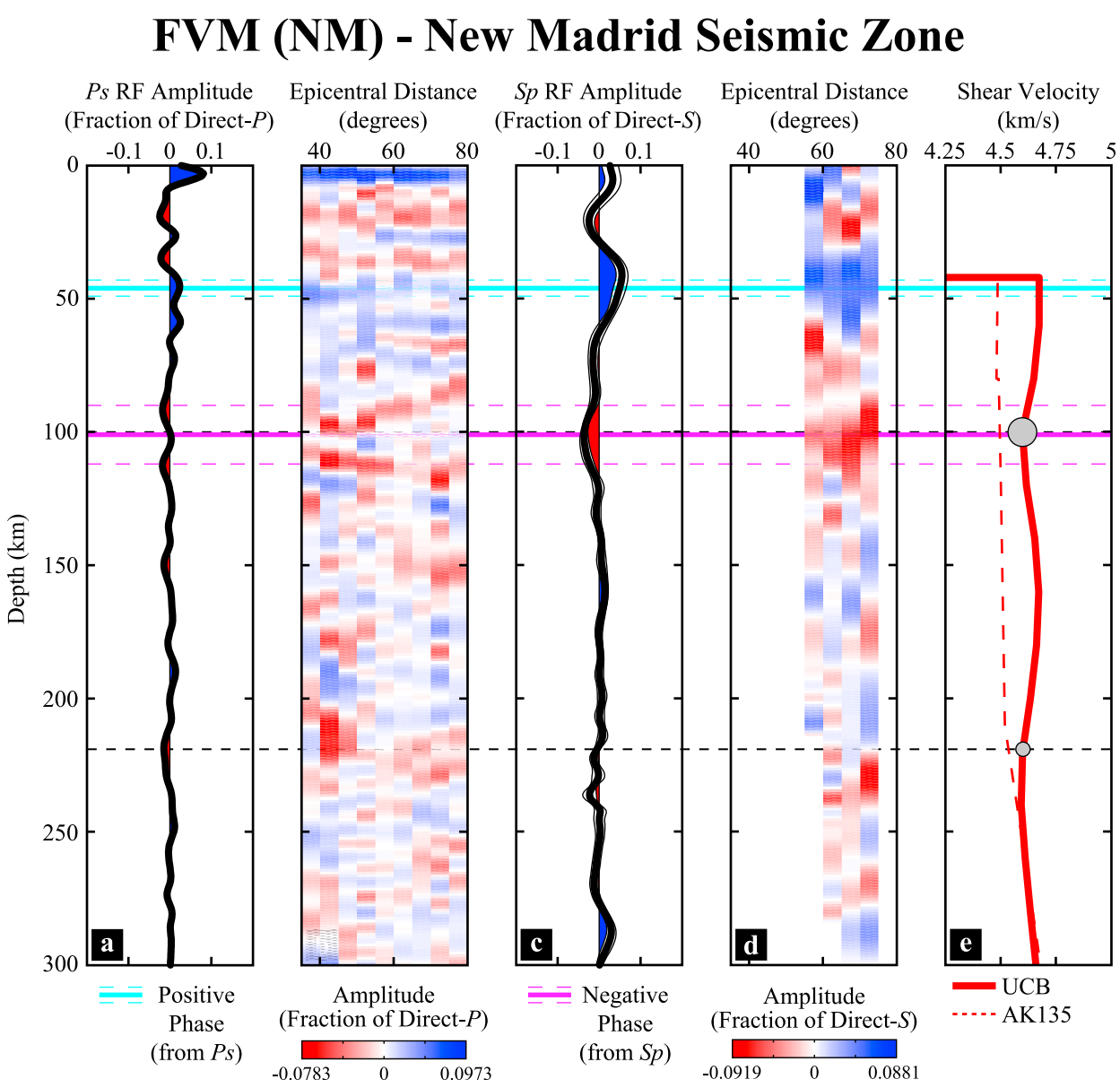

Figure 7. *Ps* and *Sp* receiver functions and V_S at station FVM. The high velocity lid is not as pronounced here as it is at ULM (Figure 5), and two low velocity zones exist (100 km and 220 km), with only a small difference in absolute velocity between the two (0.1166%; see section 4.2.4). Given the threshold difference of 0.5% (see section 4.1), the similarity between the two V_S minima does not allow us to unambiguously define the LAB from the V_S model, and therefore we do not interpret the negative *Sp* phase here (101 ± 11 km) as either the LAB or a MLD. See the caption of Figure 4 for a full explanation.

that of *Rychert et al.* [2005, 2007], the number of waveforms included and the bandpass filter used are different, which may account for the differences in the receiver functions. The *Sp* receiver functions here (Figure 6) were generated with 421 waveforms (Table 2), versus 56 waveforms used in the work of *Rychert et al.* [2007], and the bandpass filter here is 0.03–0.5 Hz, as opposed to 0.01–0.175 Hz in the work of *Rychert et al.* [2007]. In addition, the *Ps* receiver functions here employed 635 waveforms and a high frequency corner in the bandpass filter of 1 Hz, versus 123 waveforms and 2 Hz in the work of *Rychert et al.* [2005, 2007], with the result that a negative *Ps* phase at roughly 100 km is less clearly separated from Moho reverberations in this study.

4.2.4. FVM (NM): New Madrid Seismic Zone (Missouri, U.S.)

[26] Although still characterized by relatively high velocities (>3%) down to 200 km in some models, including the V_S model of *Yuan and Romanowicz* [2010] used here and *van der Lee* [2002] the New Madrid Seismic Zone and northern Mississippi Embayment are located near the margin of Proterozoic North America (what was Laurentia) where local seismic studies [*Zhang et al.*, 2009] and geochemical data [e.g., *Griffin et al.*, 2004, and references therein] suggest lower velocity lithospheric mantle may exist between 100 and 200 km. At FVM, as well as the other New Madrid (NM)

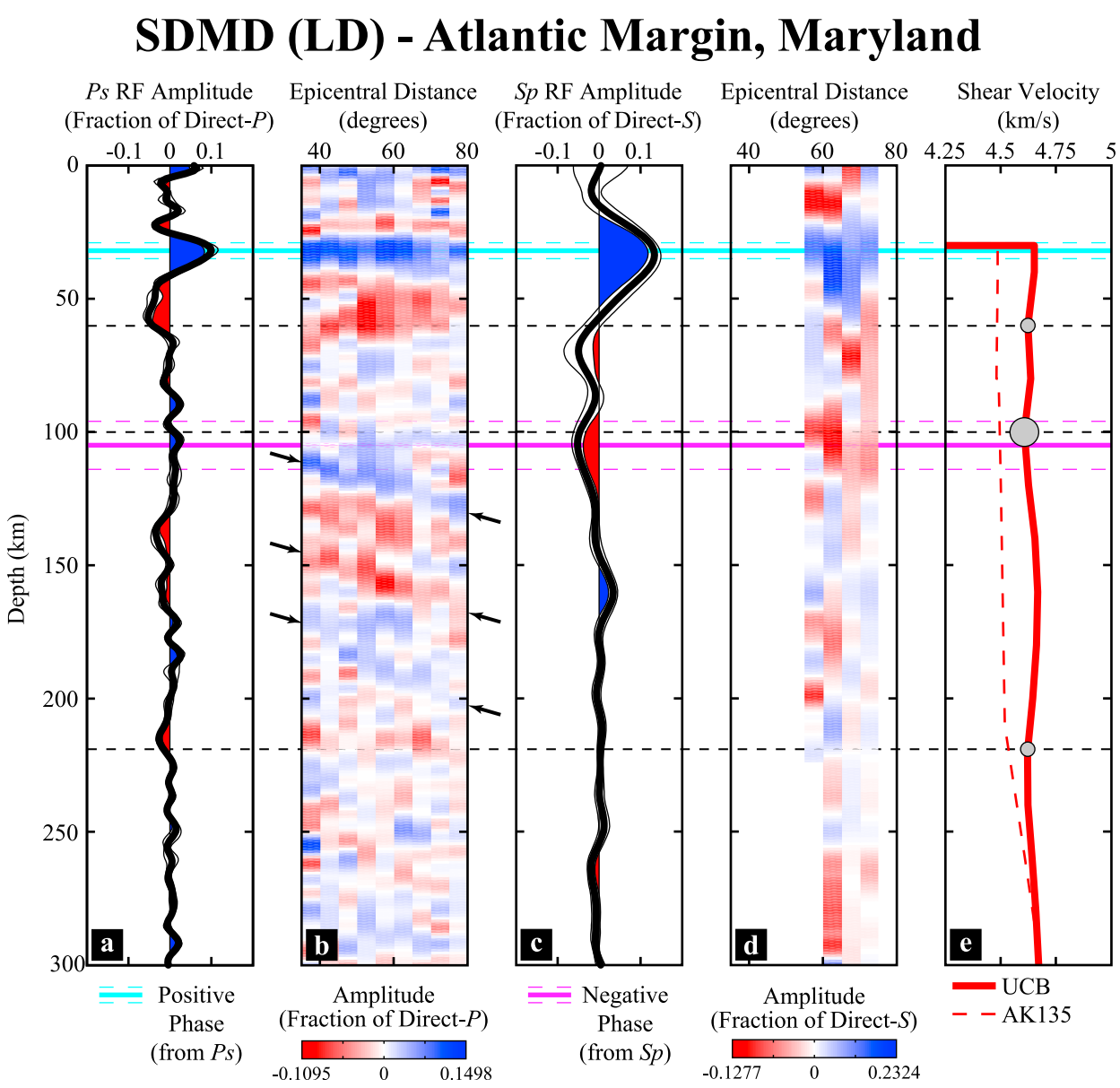

Figure 8. Detailed example of *Ps* and *Sp* receiver functions and V_S from the 3-D migration model used at station SDMD. Similar to FVM (Figure 7), the depth of the LAB from the V_S model is ambiguous, and therefore we cannot interpret the negative *Sp* phase (105 ± 9 km) as either the LAB or a MLD. See the caption of Figure 4 for a full explanation.

seismic stations (Table 2), we used the crustal model from Crust2.0 [*Bassin et al.*, 2000] because the *Ps* receiver function at crustal depths contains both a strong shallow (<10 km) conversion and multiple phases between 40 and 60 km (Figures 7a and 7b), and a reasonable H-*k* stacking result was not obtained. Nonetheless, the depth of the positive *Ps* receiver function phase (46 ± 3 km) interpreted as the Moho is in good agreement with the Crust2.0 Moho depth (42 km). It is also comparable to the Moho depth of roughly 45 km at nearby station CCM obtained from H-*k* stacking in this study (Table 2) and by *French et al.* [2009].

[27] The *Sp* receiver function shows a significant negative phase at 101 ± 11 km depth (Figure 7c). Because the V_S minima at 100 km and 220 km are nearly the same (4.5973 km/s and 4.5920 km/s; 0.1166% difference), no potential LAB depth range was defined for this station. Therefore, the discontinuity that produced the negative *Sp* phase was not interpreted as the LAB or a MLD, and was designated as "ambiguous". The shape of the absolute V_S profile at FVM is similar to V_S structure obtained in cratonic regions globally [*Romanowicz*, 2009] and the coincidence of the negative *Sp* phase with the V_S minimum near 100 km depth suggests the presence of a MLD. However, in order to maintain a consistent criterion in how the V_S profiles are interpreted (section 4.1) we retained the "ambiguous" designation.

4.2.5. SDMD (LD): Passive Atlantic Continental Margin (Maryland, U.S.)

[28] SDMD is located in central Maryland along the passive Atlantic margin of North America. Crustal thickness at

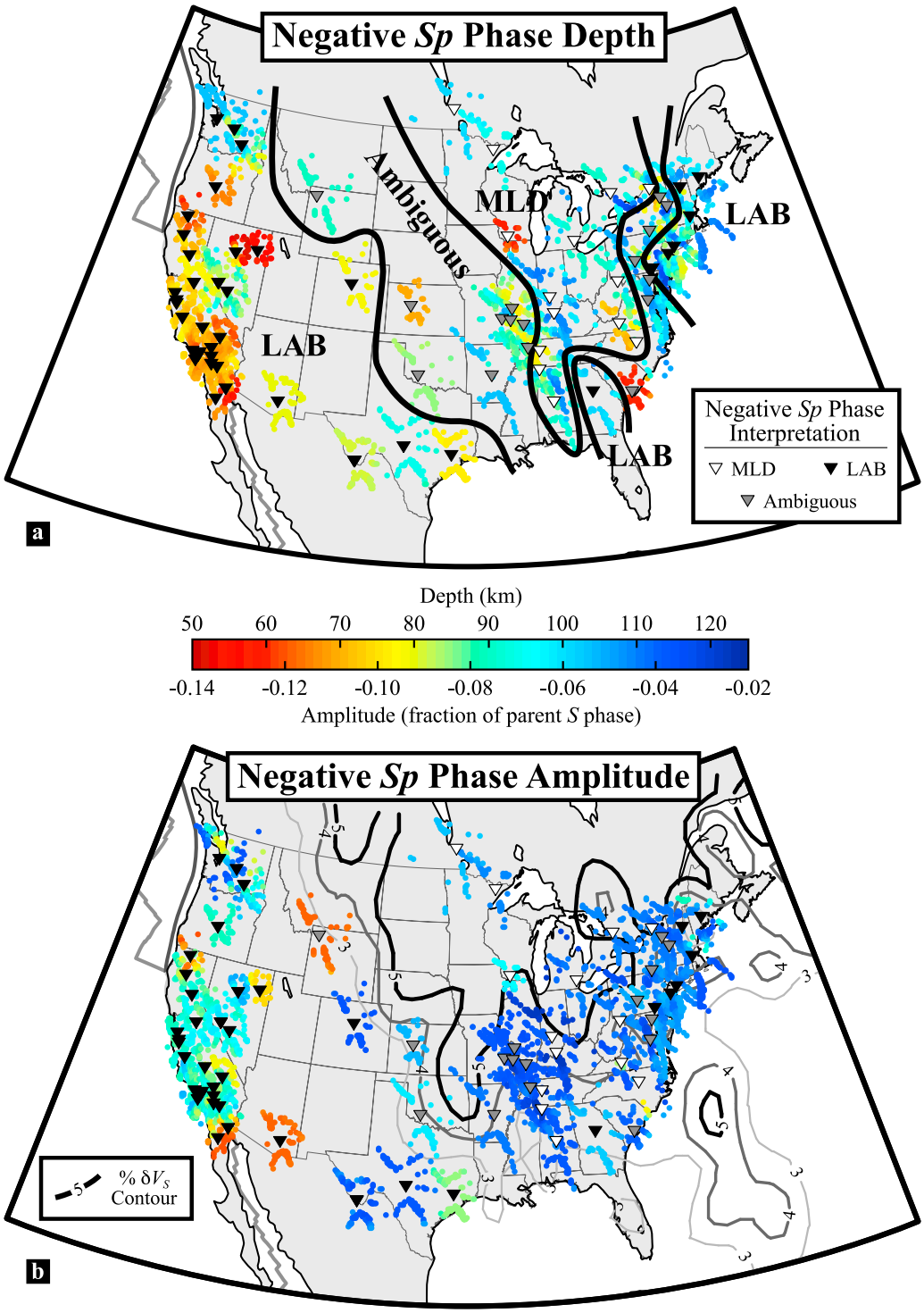

Figure 9. (a) Depths and (b) amplitudes of the prominent negative *Sp* phase from receiver functions migrated with velocity profiles extracted from the 3-D mantle model. The dots are colored for depth (Figure 9a) or amplitude (Figure 9b) and represent *Sp* piercing points that have been interpolated onto a fine grid and smoothed with a circular filter (see section 4.3 for details). Black inverted triangles indicate stations where the negative *Sp* phase is interpreted as the lithosphere-asthenosphere boundary (LAB), white inverted triangles are stations where the phase is interpreted as a mid-lithospheric discontinuity (MLD), and gray stations indicate uncertainty in the depth of the LAB from the V_S model and thus ambiguity in the interpretation of the negative *Sp* phase; thick black lines separates these regions. In Figure 9b, the 3%–5% positive velocity anomaly contours are from the V_S model at 140 km depth [*Yuan and Romanowicz*, 2010]. Among negative *Sp* phases interpreted as the LAB, the largest amplitudes are found in the western U.S. where asthenospheric velocities are lower.

SDMD was determined by H-*k* stacking to be 30 km. Both the *Ps* and *Sp* receiver functions display a strong Moho phase at 32 ± 3 km, consistent with Crust2.0 [*Bassin et al.*, 2000] (34 km) and *Chulick and Mooney* [2002] (~30 km), and crustal reverberations are clear in the *P*s distance bins (Figure 8b).

[29] We observe two negative phases in the *Sp* receiver function (70 and 105 km; Figures 8c and 8d), but because the phase at 105 ± 9 km has a larger magnitude at two standard deviations it was chosen as the phase to interpret. Most other stations along the Atlantic margin to the northeast of SDMD

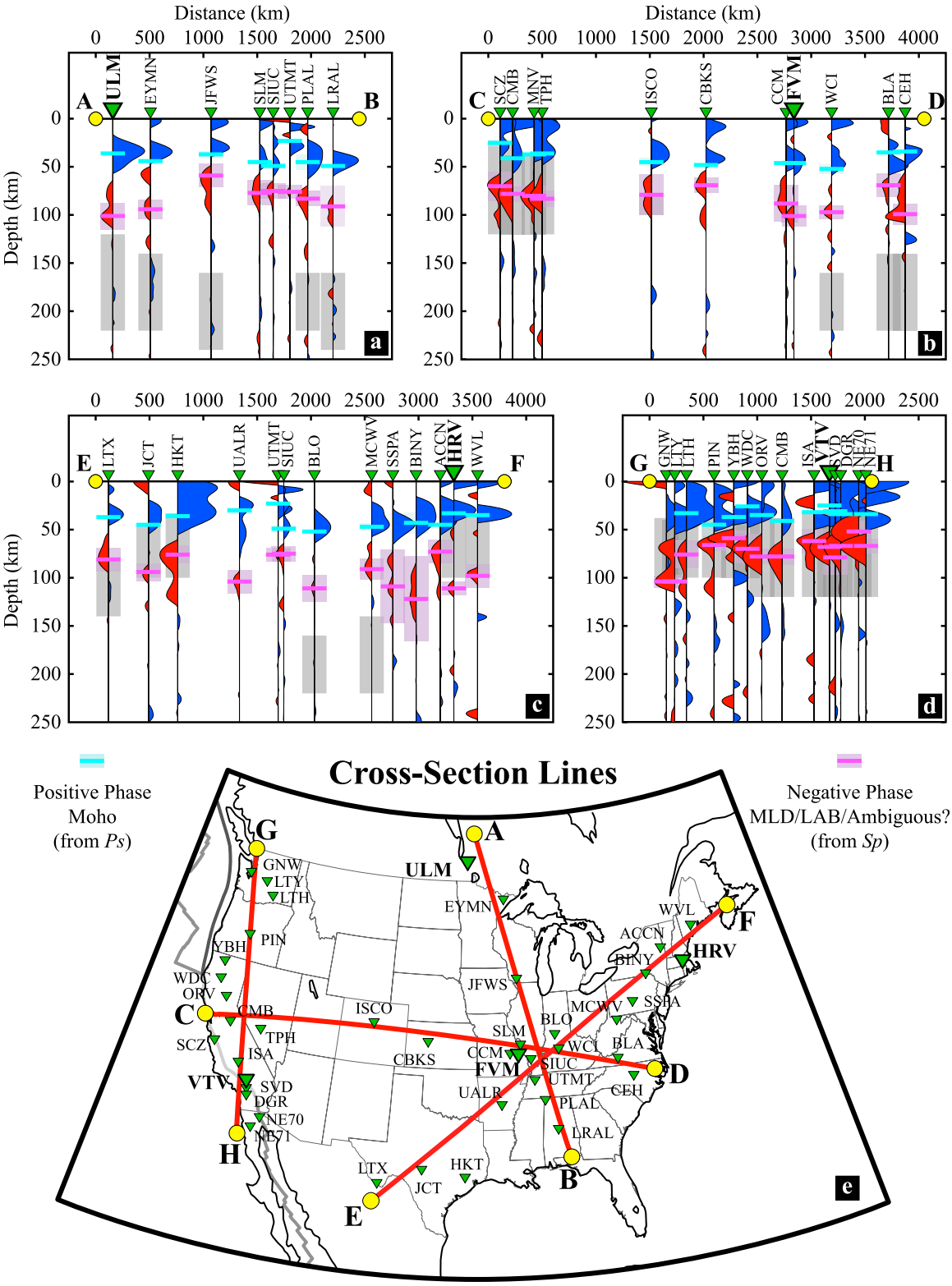

Figure 10

show a similar pattern. The absolute V_S model has three local minima, and although the V_S at 100 km is the minimum value, it is not more than 0.5% slower than the other local minima. The interpretation of the negative *Sp* phase at this station is therefore "ambiguous", rather than either a MLD or the LAB.

4.3. Negative *Sp* Phase Depths

[30] The depths of the largest negative *Sp* phase at each station are presented in map view as a smoothed function of *Sp* conversion point location (Figure 9a). We first calculated theoretical *Sp* piercing points at the depth of the chosen negative *Sp* phase (Table 2) for each station assuming the migration velocity model profile at each station (e.g., Figures 4e–8e) and then placed each piercing point onto a grid of 0.05° × 0.05° elements. (Discontinuity depths for each station are shown using the raw piercing points in auxiliary material Figure S3). Piercing points were calculated only for paths with pre-critical ray parameters at the particular interpreted discontinuity depth, resulting in ~11000 *Sp* piercing points being used. Despite the relatively fine spacing of this grid (~5.5 km), piercing points from multiple stations often fall on the same grid element, and a single depth value was calculated for each element by taking the mean of all piercing points that hit it (weighted by the individual depth errors). We introduced additional smoothing by applying a circular filter with a radius of 6 points, which yields an effective grid spacing of 0.3° (~33 km).

[31] Broadly speaking, the negative *Sp* phase depths are deeper beneath the central and eastern U.S. and shallower beneath the western U.S., although considerable variability exists within each region. For example, phases in western central Nevada are significantly deeper (85–95 km) than the rest of the western U.S. (60–70 km), and southern Wisconsin manifests the shallowest phases in the central and eastern U.S. (59 km).

[32] Although it may be tempting to conceptualize these points as a continuous surface, it is important to remember that the comparison of the receiver functions with absolute V_S leads to the interpretation of some negative *Sp* phases as the LAB and others as a MLD (black versus white stations in Figure 9), and some negative *Sp* phases cannot be unambiguously interpreted (gray stations in Figure 9). Within the tectonically active western U.S., the discontinuity lies within the transition to a very slow asthenosphere, and corresponds to the LAB. At stations in Phanerozoic terranes in Texas, Georgia, and most of the northeastern U.S., the discontinuity also appears to be the LAB. Within the cratonic regions of central North America (Figure 1), the thick high velocity lid (see V_S contours in Figure 9b) and shallow *Sp* phases point to an interpretation of the discontinuity as a MLD. The V_S model in the region separating the LAB and MLD regions contains at least two low velocity zones of comparable magnitude, and therefore, the negative *Sp* phases there could arguably be attributed to either the LAB or an MLD. However, this ambiguous region does not necessarily, or even likely, represent a smooth transition with a continuous discontinuity between the LAB and MLD regions.

4.4. *Sp* Negative Phase Amplitude Variations

[33] Using the same gridding and smoothing technique employed with the negative *Sp* phase depths (section 4.3), we also present the variation of negative *Sp* phase amplitude (Figure 9b). Similar to the depth of the negative *Sp* phases (Table 2), the difference in amplitude between the receiver functions migrated with the 3-D and 1-D mantle models are virtually indistinguishable, and here only the amplitudes based on the 3-D model are shown. Unlike the depths of the prominent negative *Sp* phase (Figure 9a), the amplitudes show a clear distinction between larger negative amplitudes (red and green) in the western U.S. and smaller amplitudes (blue) in the central and eastern U.S. A rough correlation exists between depth (Figure 9a) and amplitude (Figure 9b); deeper phases tend to have smaller amplitude.

[34] For stations where the negative *Sp* phase is interpreted as the LAB, the larger amplitude in the western U.S. implies that the velocity contrast between the lithospheric lid and asthenosphere is larger or occurs as a more rapid velocity gradient than in the eastern U.S. The absolute V_S model contains much slower velocities at asthenospheric depths in the western U.S. than in the eastern U.S. (see for example the velocity anomaly contours for a depth of 140 km in Figure 9b, or contrast the VTV and HRV V_S profiles in Figures 4 and 6). This result suggests that the apparently larger LAB velocity contrasts in the western U.S. are due to a much slower asthenosphere.

4.5. Selected Cross-Sections

[35] Presentation of all receiver functions in the format of Figures 4–8 is not practical, but we include four cross-sections (Figure 10) that illustrate more than half of our picked *Sp* receiver functions relative to the Moho and negative *Sp* phase depths (cyan and magenta lines, respectively) and the inferred LAB depth from the V_S model (gray regions).

Figure 10. Cross-sections illustrating the relationship between *Sp* receiver functions and both Moho (cyan line in Figures 10a–10d) and negative *Sp* phase (magenta line in Figures 10a–10d) depths. The LAB depth range inferred from the V_S model, when unambiguous, is shown by the gray shaded regions in Figures 10a–10d (see section 4 and caption of Figure 4 for explanation). In general, the negative *Sp* phases are located between 60 and 100 km. In the western and northeastern U.S., as well as some stations in the southeast, the inferred transition from the minimum V_S up to the next peak in V_S falls in this same depth range, and we interpret the negative *Sp* phases in these regions to represent the conversion of energy at the LAB. In contrast, the transition from the LVZ to the higher velocity lid beneath the central U.S. occurs at roughly 200 km, and here the negative *Sp* phases are interpreted at a MLD. The receiver functions in each cross-section are plotted at the same scale, and their amplitudes show the smallest positive (blue) and negative (red) values required at 95% confidence (2σ uncertainties have been stripped off of the bootstrap mean). The larger amplitude of the negative *Sp* phases along the west coast (Line G-H, Figure 10d) relative to other regions is easily observed. A detailed description of each cross-section can be found in section 4.4. Only stations shown in Figures 10a–10d are plotted on the reference map in Figure 10e with the cross-section lines. Auxiliary material Figure S4 shows these same receiver functions down to 400 km depth.

For clarity and in contrast to the examples in Figures 4–8, Figure 10 shows only receiver function amplitudes within the two standard deviation uncertainties from the bootstrap testing (i.e., only resolved positive (blue) and negative (red) amplitudes).

4.5.1. Cross-Section A-B (ULM-LRAL)

[36] The first cross-section (A-B, Figure 10a) runs south from station ULM within the Superior craton in southern Manitoba, Canada through the New Madrid Seismic Zone and to station LRAL in Alabama. The Moho (positive *Ps* phase) shows a slight increase in depth from ~40 km near ULM to ~50 km near LRAL. The negative *Sp* phase decreases in depth from 101 ± 14 km at ULM to 59 ± 12 km beneath JFWS before increasing again towards LRAL (91 ± 21 km). This shallowing would be less prominent if the deeper (and smaller) phase observed at JFWS had been picked as the primary arrival. In any case, the depth of the *Sp* phase at all of these stations lies well above the potential LAB depth ranges from the V_S model where they exist (gray regions in Figure 10a). The phases are interpreted as a MLD, except at SLM, SIUC and UTMT which fall into the "ambiguous" category. Overall, very little converted energy is seen at depths greater than 100 km.

4.5.2. Cross-Section C-D (SCZ-CEH)

[37] Cross-section C-D (Figure 10b) spans the continental U.S. from central California to North Carolina. The crust is relatively shallow beneath SCZ (25–30 km) and gradually thickens to ~55 km across the Basin and Range, through the Great Plains, and into the southern Appalachians before thinning again to ~35 km in eastern North Carolina. Although our resolution is lower, these values agree well with those presented by *Chulick and Mooney* [2002]. In contrast with the Moho, the negative *Sp* phases show a moderate amount of variability, ranging between 70 and 100 km. West of Colorado (station ISCO), amplitudes of the negative *Sp* phases are larger and their depths agree with the likely LAB range from absolute V_S (gray regions). The LAB appears to deepen in the western Basin and Range at stations MNV and TPH (also see Figure 9a), but the eastern extent of this apparently thicker lithosphere is not well-constrained because no piercing points exist east of TPH until ISCO. East of WCI, the V_S model indicates a thicker high velocity lid (~200 km) but the negative *Sp* phases are at depths of ~70–100 km, resulting in their interpretation as a MLD. No eastern stations in this profile have significant negative *Sp* energy within the highlighted LVZ-to-lid transition region.

4.5.3. Cross-Section E-F (LTX-WVL)

[38] Cross-section E-F (Figure 10c) crosses from Phanerozoic lithosphere in Texas, through the Proterozoic terranes in the central U.S., to the Paleozoic Appalachians in the northeastern U.S. The negative *Sp* phases show significant variability but no significant negative *Sp* energy exists between 150 and 250 km across the line. The V_S model indicates a thin lithosphere (50–100 km) at either end of this line and a thick lithosphere (150–200 km) near its center at BLO and MCWV (gray regions), but the LAB depth is unclear in both the New Madrid Seismic Zone (stations UALR, UTMT, and SIUC) and the central Appalachians (stations SSPA and BINY). Therefore, the negative *Sp* phases are interpreted as the LAB near the Atlantic margin and as a MLD in a portion of the Proterozoic craton, but are not interpreted in between.

4.5.4. Cross-Section G-H (GNW-NE71)

[39] The last cross-section (G-H, Figure 10d) differs from the first three in that it follows the tectonically and volcanically active western margin of the U.S. (i.e., Cascadia, the eastern Sierras, and southern California). Along this profile, the negative *Sp* phases fall within the potential LAB depth range from the V_S model and are interpreted as the LAB, with the caveat that it may be difficult to distinguish the LAB from discontinuities associated with the Juan de Fuca slab in the Pacific Northwest (stations GNW, LTY, PIN, YBH). An obvious feature of these receiver functions is the large amplitude of the negative *Sp* phases, indicating a greater velocity contrast at the LAB than is typical of the eastern U.S. In addition, more energy appears at larger depths than in other profiles. These deeper phases may represent real structure and are not unexpected given the likelihood of vertical heterogeneity associated with recent and current subduction of the Juan de Fuca/Farallon Plate and processes such as lithospheric delamination beneath the Sierras [e.g., *Zandt et al.*, 2004]. *Li et al.* [2007] also investigated this same general region with *Sp* receiver functions, and our results here do not differ significantly from theirs; the only major discrepancy appears to be near TPH and MNV, where they image a shallower LAB (60 km versus 80–83 km obtained here; see cross-section C-D, Figure 10b).

5. Discussion

[40] A growing body of studies that employ *Sp* and *Ps* receiver functions have found evidence for discontinuities characterized by a significant negative velocity contrast at depths comparable to those documented here (*Rychert et al.* [2010] and *Fischer et al.* [2010] give reviews). These studies span oceanic regions [*Li et al.*, 2000; *Collins et al.*, 2002; *Li et al.*, 2004; *Kumar et al.*, 2005b; *Vinnik et al.*, 2005; *Wölbern et al.*, 2006; *Heit et al.*, 2007; *Kumar et al.*, 2007; *Kawakatsu et al.*, 2009; *Rychert and Shearer*, 2009], regions of relatively thin (<120 km) continental lithosphere [*Oreshin et al.*, 2002; *Kumar et al.*, 2005a; *Rychert et al.*, 2005, 2007; *Chen et al.*, 2006; *Mohsen et al.*, 2006; *Sodoudi et al.*, 2006a, 2006b; *Hansen et al.*, 2007; *Heit et al.*, 2007; *Kumar et al.*, 2007; *Li et al.*, 2007; *Ozacar et al.*, 2008; *Rychert and Shearer*, 2009; *Chen*, 2009], and continental regions with thicker cratonic-style lithosphere [*Bostock*, 1998; *Ford et al.*, 2009; *Rychert and Shearer*, 2009]. A widely distributed layer of low velocities at roughly 100 km depth beneath continents has also been argued for on the basis of long-range active source profiles [e.g., *Thybo and Perchuc*, 1997; *Thybo*, 2006] and absolute V_S models from global surface-wave tomography [*Romanowicz*, 2009]. However, in some cratonic regions deeper discontinuities (>150 km) have also been proposed by *Sp* and *Ps* studies [*Sacks et al.*, 1979; *Kumar et al.*, 2007; *Wittlinger and Farra*, 2007; *Savage and Silver*, 2008; *Snyder*, 2008; *Hansen et al.*, 2009].

[41] Here we discuss possible physical and chemical mechanisms that could produce a negative velocity contrast and be responsible for the discontinuity that we have imaged beneath the continental U.S. and small portions of Mexico and Canada. We first explore the origin of this feature in regions where we have interpreted it as the LAB and then in regions of thicker lithosphere where we have interpreted it as a MLD (Table 2).

5.1. Negative Velocity Contrast at the Lithosphere-Asthenosphere Boundary

[42] Where interpreted as the LAB, the depth of the discontinuity imaged in this study varies from 51 km to 111 km (black stations in Figure 9, Table 2). In addition, the amplitude of the *Sp* phase marking the discontinuity is significantly larger in the tectonically active western U.S. than within the Phanerozoic terranes along the southern and eastern margins of Proterozoic North America (Figure 9b), a result that correlates with lower asthenospheric shear velocities in the west.

[43] Some studies conclude that temperature, or a combination of temperature and grain size, can largely explain the transition from fast lithosphere to slow asthenosphere [e.g., *Faul and Jackson*, 2005; *Stixrude and Lithgow-Bertelloni*, 2005; *Priestley and McKenzie*, 2006]. Other studies emphasize the faster velocities expected in dry, depleted lithosphere, versus more hydrated and fertile asthenosphere [*Hirth and Kohlstedt*, 1996; *Karato and Jung*, 1998; *Gaherty et al.*, 1999]; however, the amount of shear velocity drop that can be attributed to partial melting-induced depletion is the subject of debate [*Lee*, 2003; *Schutt and Lesher*, 2006]. The presence of a small amount of partial melt in the asthenosphere could dramatically reduce its shear velocity, although the magnitude of the effect strongly depends on the melt distribution geometry [e.g., *Gribb and Cooper*, 2000; *Hammond and Humphreys*, 2000; *Takei*, 2002; *Faul et al.*, 2004; *Kawakatsu et al.*, 2009]. Rapid variations in anisotropy with depth may also create discontinuities [e.g., *Bostock*, 1998; *Gaherty et al.*, 1999; *Levin and Park*, 2000; *Gung et al.*, 2003]. Considering these possibilities, what can we postulate about the source of the negative *Sp* phase where we interpret it on our receiver functions as the LAB?

[44] The amplitudes of *Sp* and *Ps* phases are largely controlled by the gradient in shear velocity at the discontinuity where they are generated [e.g., *Rychert et al.*, 2007, 2010]. To accurately bound the shear velocity gradient, detailed waveform modeling is required [e.g., *Collins et al.*, 2002; *Rychert et al.*, 2005, 2007; *Chen et al.*, 2006; *Li et al.*, 2007; *Kawakatsu et al.*, 2009; *Ford et al.*, 2009], and such an effort with the data gathered in this study will be the focus of a future investigation. Nonetheless, existing modeling provides some guidelines that we can apply to the results shown here.

[45] *Rychert et al.* [2007] jointly modeled *Ps* and *Sp* receiver functions in the northeastern U.S. and southeastern Canada and determined that the LAB velocity gradient corresponded to a 5–10% drop in shear velocity over 5–11 km. Even when accounting for anelastic (viscoelastic relaxation or attenuation) effects on shear wave velocity [*Faul and Jackson*, 2005], the minimum temperature gradient required at the LAB to match these velocity gradients (20°C/km) is larger than temperature gradients at the base of the lithosphere from geodynamical models in which viscosity depends solely on temperature and pressure [e.g., *King and Ritsema*, 2000; *Cooper et al.*, 2004]. *Chen et al.* [2006] arrived at a similar conclusion from their modeling of *Ps* receiver function data in eastern China. In both cases [*Rychert et al.*, 2005, 2007; *Chen et al.*, 2006], the additional velocity reduction was explained by the presence of water or melt in the asthenosphere, possibly in combination with greater depletion in the lithosphere or (in the case of *Rychert et al.* [2007]) a small contribution from depth variations in anisotropy.

[46] When *Sp* phases alone are considered, constraints on the velocity gradient that generated the phase are typically looser, due to the longer dominant periods in *Sp* receiver functions. *Ford et al.* [2009] calculated *Sp* receiver functions for stations in Phanerozoic eastern Australia using waveform rotation, deconvolution, filtering and migration approaches identical to those employed here, resulting in the same *Sp* dominant periods (10–11-s). With waveform modeling that accurately accounted for the ray parameter of each *Sp* phase in the observed receiver functions, *Ford et al.* [2009] found that best-fitting LAB velocity gradients in eastern Australia ranged from a 5% velocity decrease over 0 km to a 10% decrease over 30 km; gradients distributed over more than 40 km could be ruled out if velocity drops are limited to no more than 10%, even when the 2σ uncertainties on the observed receiver functions are taken into account. 10% is greater than the total shear velocity drop from lithosphere to asthenosphere seen in surface wave models [*Gaherty et al.*, 1999; *Nettles and Dziewonski*, 2008; *Romanowicz*, 2009; *Yuan and Romanowicz*, 2010]. When the acceptable velocity gradients are scaled to temperature gradients using the relationships of *Faul and Jackson* [2005] and the approach of *Rychert et al.* [2007], the resulting temperature gradient magnitudes include values comparable to temperature gradients found at the base of the lithosphere in geodynamical models that span thick cratonic lithosphere and thinner lithosphere around its margins [e.g., *King and Ritsema*, 2000; *Korenaga and Jordan*, 2002; *Cooper et al.*, 2004]. However, in these models, the increase in temperature from lithosphere to asthenosphere is distributed over vertical distances of more than 70 km. Therefore, *Sp* phases generated by velocity gradients that are localized in depth to 30–40 km or less do not appear to be compatible with models in which temperature alone creates the LAB.

[47] The amplitudes and dominant periods of the negative *Sp* phases interpreted as the LAB in this study are comparable to those modeled by *Ford et al.* [2009] and *Rychert et al.* [2007]. Therefore, it is reasonable to conclude that they were generated by LAB velocity gradients that are localized in depth over 30–40 km or less, although this conclusion will be tested in the future with detailed waveform modeling that matches the specific phase path distributions at each station. In the Phanerozoic eastern U.S., where comparable geodynamical models predict only moderate mantle upwelling and broad thermal gradients between the lithosphere and asthenosphere [*King and Ritsema*, 2000; *Korenaga and Jordan*, 2002; *Cooper et al.*, 2004], the presence of LAB *Sp* phases (Figure 9a) likely indicates that the asthenosphere is significantly hydrated relative to the lithospheric mantle or contains a small amount of partial melt.

[48] Could melt be present beneath the continental lithosphere in the eastern U.S.? When *Mierdel et al.* [2007] jointly considered water solubility in Al-saturated enstatite and olivine, they showed that a minimum in water solubility occurs at depths of 100 km (for a typical old oceanic geotherm) to 150 km (for relatively cold continental geotherms), leading them to infer that melting would occur beneath the continental lithosphere in the presence of a few hundred parts per million of water. *Elkins-Tanton et al.* [2008] concluded that small percentages of partial melt could exist in the asthenosphere beneath eastern North America (1–2% melting for an asthenosphere with a mantle potential temperature of

1400°C and 150–300 ppm H_2O, or a potential temperature of 1350°C with 450–900 ppm H_2O). In these models, the LAB is inferred to be a "damp" solidus, and therefore may correspond to a permeability barrier that would trap melt within the asthenosphere. In addition, melt that was able to migrate above the LAB would crystallize relatively quickly, assuming melt bodies with reasonable dimensions [*Elkins-Tanton et al.*, 2008].

[49] In contrast to eastern U.S. stations, the negative *Sp* phases at western U.S. stations display larger amplitudes (Figure 9b), likely due to lower asthenospheric velocities, as seen in the V_S model [*Yuan and Romanowicz*, 2010] and other seismological studies [e.g., *Grand*, 1994; *Humphreys and Dueker*, 1994; *van der Lee and Nolet*, 1997; *van der Lee*, 2002; *Godey et al.*, 2004; *Marone et al.*, 2007; *Xue and Allen*, 2007; *Li et al.*, 2008; *Nettles and Dziewonski*, 2008; *Roth et al.*, 2008]. By analogy with the modeling results of *Ford et al.* [2009], these negative *Sp* phases imply velocity gradients distributed over less than 30 km in depth for velocity drops of no more than 10%. Other geophysical and geological observations in the western U.S., such as high heat flow [*Lachenbruch*, 1978; *Morgan and Gosnald*, 1989; *Blackwell et al.*, 1991], Basin and Range extension [*McKenzie and Bickle*, 1988; *Wernicke et al.*, 1988; *Bennett et al.*, 1998], dynamic topography [*Lowry et al.*, 2000], and a plethora of recent and active volcanism (e.g., the Cascade arc, High Lava Plains, Yellowstone hotspot track, Long Valley Caldera), indicate the shallow upper mantle is anomalously hot and, at least in certain regions, likely partially molten. Owing to this well-established view of the western U.S., it is reasonable to attribute the larger amplitude of negative *Sp* phases in this region to a high temperature, partially molten asthenosphere underlying a relatively melt-free lithosphere. However, very strong LAB temperature gradients due to small-scale convection, plus the effects of asthenospheric water, cannot be ruled out. These interpretations require testing with detailed modeling of the LAB velocity gradient and focused geodynamical studies.

5.2. Absence of a Sharp LAB Beneath Thick Lithosphere

[50] A key result of this study is the apparent absence of a sharp gradient in shear velocity beneath all regions of the North American continent where absolute V_S structure indicates a seismic lid of more than 130 km in thickness. These include the sampled Archean and Proterozoic craton, as well as portions of the Phanerozoic Appalachian orogen in the eastern U.S. (Figures 1 and 9). This finding contrasts with other cratonic regions where *Sp* receiver functions have been used to infer an observable LAB discontinuity at depths of more than 160 km [*Sacks et al.*, 1979; *Kumar et al.*, 2007; *Wittlinger and Farra*, 2007; *Hansen et al.*, 2009]. Elsewhere in North America, a sharp LAB has been invoked beneath the Slave Craton [*Snyder*, 2008], although this study employed *Ps*, rather than *Sp*, receiver functions.

[51] A valid question is whether significant lateral variations in LAB depth or overlying mantle structure may have obscured the observation of *Sp* phases from the base of the cratonic lithosphere in this study. *Sp* conversion points at depths comparable to the cratonic LAB span a significant area around each station. Significant variations in discontinuity depth over this area would reduce the coherence of the phase during simultaneous deconvolution, as would strong lateral variations in mantle V_P/V_S. However, to cancel out an LAB discontinuity, these variations would need to be large, on the order of 25 km or more for LAB depth, and more than the total range of V_P/V_S spanned by the combined V_P [*Burdick et al.*, 2008] and V_S [*Yuan and Romanowicz*, 2010] models used in this study. To assess the presence of such effects in data, we calculated receiver functions for narrow back-azimuthal ranges at the 7 cratonic stations with MLD phases and more than 80 Sp waveforms (ULM, SADO, WCI, WVT, BLO, AAM, JFWS). Most of these back-azimuthal bins contained too few data to produce meaningful receiver functions, but in a few cases, receiver functions from 30 or more waveforms per bin at back-azimuths of 330° to 350° and 155° to 175° were interpretable. None of these examples showed a clear, isolated negative *Sp* arrival below the MLD to depths of 230 km, the depth interval that contains the potential LAB depth range from absolute V_s for cratonic stations. Of course, if LAB depth or mantle V_P/V_S greatly varied at scales even smaller than the volumes sampled by the narrow back-azimuthal ranges, they could still lead to phase incoherence.

[52] Assuming that large lateral LAB depth and V_P/V_S variations beneath individual stations are not present, the absence of significant *Sp* phases from the regions of thick lithosphere sampled in this study implies that the velocity drop at the LAB is very weak and/or gradual in depth. However, the V_S model at most cratonic stations indicates a significant drop in velocity from the fast lid to the asthenosphere. For example, at ULM, this velocity drop is 4% (Figure 5e). Therefore, the lack of *Sp* energy from the LAB likely represents a gradual velocity gradient. How gradual would this gradient have to be? Using synthetic *Sp* receiver functions at comparable periods of 10–11 s, *Ford et al.* [2009] showed that velocity drops of 4–10% did not produce clear *Sp* phases when they were distributed over vertical distances of 70 km or more; *Sp* phases from 50 km gradients were just at the edge of being observable given typical signal-to-noise levels. We therefore conclude that the shear velocity gradient beneath the thick North American lithosphere likely occurs over 50–70 km or more in depth, although this finding requires confirmation from waveform modeling specific to the *Sp* paths in this study. The relatively gradual temperature gradients predicted by geodynamical models where viscosity depends only on temperature and pressure [*King and Ritsema*, 2000; *Cooper et al.*, 2004] are therefore a viable option in these regions of the continent. However, gradients in mantle hydration or melt content distributed over 50–70 km or more cannot be ruled out.

5.3. Negative Velocity Contrast Within the Lithosphere

[53] Given that significant negative discontinuities appear to exist at depths of 59–113 km in the lithosphere of cratonic North America and certain portions of the Phanerozoic eastern U.S., what are the possible sources of the velocity contrasts accompanying this layering? Here we evaluate the mechanisms presented in the previous section and some additional possibilities, in light of likely geotherms for the region. Moreover, because a discontinuity corresponding to the top of a low velocity layer internal to the cratonic lithosphere has been proposed in other cratonic regions [*Savage and Silver*, 2008; *Ford et al.*, 2009] as well as in cratons globally [*Thybo and Perchuc*, 1997; *Thybo*, 2006; *Rychert*

and Shearer, 2009; *Romanowicz*, 2009], the conclusions drawn here have implications beyond North America.

[54] *Thybo* [2006] argues that a lowering of the peridotite solidus by the presence of water and/or carbon dioxide is likely responsible for a mid-lithospheric LVZ at depths of roughly 100 km through the effects of partial melt (if temperatures are above the solidus) or by a decrease in shear modulus and increase in attenuation at sub-solidus temperatures [*Sato et al.*, 1989a, 1989b]. Within the cratonic regions sampled in our study, the geotherms preferred by *Griffin et al.* [2004] based on peridotitic garnet xenocrysts imply temperatures below 800°C at depths of 100 km. These values are below even the lowest temperature estimates for the water-saturated solidus [e.g., *Katz et al.*, 2003; *Grove et al.*, 2006], making the present-day existence of melt unlikely. Allowing for warmer cratonic geotherms at 100 km, for example the higher temperature end of the 750–900°C range inferred for the craton from seismic velocities [*Goes and van der Lee*, 2002] or 900–1100°C from heat flow [*Artemieva and Mooney*, 2001], melt or near-solidus conditions might exist in the presence of water contents approaching saturation. In addition, the highest of these values (1100°C) just reaches the solidus for natural carbonated peridotite at 100 km [*Dasgupta and Hirschmann*, 2006]. Hydration of the North American lithosphere by flat-slab subduction of the Farallon Plate in the early Cenozoic has been proposed to explain widespread uplift and volcanism in the western U.S. [*Humphreys*, 1995; *Humphreys et al.*, 2003], and the Farallon slab has been proposed as a source of volatile-enrichment in the central and eastern U.S. asthenosphere [*van der Lee et al.*, 2008]. However, these scenarios raise the question of how volatiles would have become highly concentrated in a layer whose top lies at 70–115 km, and how this layer was maintained over time; one possibility is the rapid increase in olivine and Al-saturated enstatite water solubility at roughly 100 km predicted for a cold, cratonic geotherm [*Mierdel et al.*, 2007]. In addition, recent modeling of surface motions in response to glacial isostatic adjustment [*Peltier and Drummond*, 2008] favors a lower-lithospheric layer of reduced viscosity (10^{22} Pa s) from 60–100 km depth that relaxes a large fraction of horizontal stress and reduces misfits to observed horizontal motions. This type of weak zone could be taken as evidence for a layer of melt or highly hydrated mantle.

[55] Another reasonable scenario is that the *Sp* discontinuity represents the sharp top of a now-solid melt cumulate layer, whose lower boundary is more gradual, and therefore does not produce its own observable phase. At depths comparable to the observed MLD, the cumulate could be pyroxenite, whose velocity would be sufficiently slow with respect to peridotite [*Stixrude and Lithgow-Bertelloni*, 2005; *Behn and Kelemen*, 2006; C.-T. Lee, personal communication, 2009]. This melt layer could have been created at an earlier time when the cratonic lithosphere was warmer, allowing water-rich melts from the asthenosphere to percolate up through the lithosphere and collect in a layer whose top would have been the wet pyroxenite solidus. To explain the 4.5% drop in velocity they image at 150 km depth in the Kalahari craton, *Savage and Silver* [2008] propose that infiltration of basaltic melt and metasomatic fluids refertilized and reduced velocity in the originally depleted mantle of the cratonic lithosphere, and that the sharp top of this slow layer corresponds to the basalt liquidus at the time the melts were present. While a mantle refertilization process could have played a role in creating slow velocities internal to the North American lithosphere, the basalt liquidus [*Yasuda et al.*, 1994; *Médard and Grove*, 2008] would likely have been too hot relative to a cratonic geotherm at MLD depths to provide a general mechanism for the MLD observed in this study.

[56] Anisotropic fabric is another plausible mechanism for generating a velocity contrast within the lithosphere. A change in anisotropy, either between two regions with different orientations of anisotropy or between an isotropic and an anisotropic region, should be observable with receiver functions [e.g., *McNamara and Owens*, 1993; *Levin and Park*, 1997; *Nagaya et al.*, 2008] as variations in phase amplitude timing with back-azimuth and including the presence of converted SH phases. Although rigorous analysis of evidence for anisotropy in the receiver functions presented in this study is reserved for future work, a number of teleseismic converted phase studies have argued for anisotropic layering within thick cratonic lithosphere [*Bostock*, 1998; *Levin and Park*, 2000; *Saul et al.*, 2000; *Wittlinger and Farra*, 2007; *Mercier et al.*, 2008; *Snyder*, 2008], sometimes associating discontinuities in the 70–115 km depth range with the Hales discontinuity [*Bostock*, 1998; *Levin and Park*, 2000; *Snyder*, 2008]. The original definition of the Hales discontinuity involved an increase in isotropic velocity with depth [*Hales*, 1969], as opposed to the decreases in velocity at the MLD found in this study. However, if a discontinuity involves anisotropy, the apparent sign of the discontinuity may vary as a function of sampling with back-azimuth.

[57] In the Canadian Shield, north of our study region, *Ps* receiver function imaging, along with xenolith and reflection data, has been used as evidence for significant lithospheric layering that resulted from stacking of oceanic plates during paleo-Proterozoic subduction [*Cook et al.*, 1997; *Bostock*, 1998; *Mercier et al.*, 2008; *Snyder*, 2008]. In particular, a thin (10 km) anisotropic layer inferred to be the top of a subducted slab was observed at depths of 30–90 km beneath the Wopmay orogen and the Slave craton [*Bostock*, 1998; *Mercier et al.*, 2008], overlapping the range of MLD depths found in this study (59–113 km), and deeper anisotropic discontinuities were found further to the west beneath the Slave craton [*Snyder*, 2008]. Anisotropic layering has also been documented in the lithosphere of the Arabian Shield at 70 km depth [*Levin and Park*, 2000] and the Indian Shield at 90 km depth [*Saul et al.*, 2000]. The existence of such anisotropic layering within the Proterozoic mobile belts of the central and eastern U.S. has not been established by receiver function studies. However, using surface wave tomography, *Yuan and Romanowicz* [2010] found a vertical shift in the fast direction of azimuthal anisotropy at depths of 50–150 km across the North American craton, as well as a deeper change in azimuthal anisotropy with depth that they associate with the LAB. *Yuan and Romanowicz* [2010] interpret the shallowest layer of azimuthal anisotropy as the oldest, most highly depleted cratonic lithosphere, and the second layer of azimuthal anisotropy as a layer of less depleted lithosphere that accreted at a later time. If the boundary between these layers is sufficiently sharp in depth, it could represent another mechanism for the MLD *Sp* phases found in this study at 60–110 km.

[58] The spinel-garnet transition was also evaluated as a possible cause of the MLD observed in our data. However,

while this phase boundary occurs at approximately the correct depth, and the deeper phase (garnet) does have a slower velocity, the relatively small percent of spinel in a peridotite mantle lithosphere would make the velocity contrast associated with this transition too small to explain the observed MLD [*Stixrude and Lithgow-Bertelloni*, 2005; G. Hirth, personal communication, 2009].

6. Conclusions

[59] Recent studies propose that a global discontinuity between 80 and 120 km with a negative velocity contrast exists [e.g., *Thybo*, 2006; *Rychert and Shearer*, 2009; *Romanowicz*, 2009]. The *Sp* receiver functions presented here also reveal at least one discontinuity with a negative velocity gradient beneath most of the continental U.S. (and portions of Mexico and Canada) at a similar depth (Figure 9). However, comparison of this discontinuity to absolute shear-wave velocities leads to its interpretation as the LAB in the western U.S. and portions of the Phanerozoic eastern U.S. and as a MLD in the cratonic core of the continent and certain Phanerozoic regions.

[60] In the tectonically active western U.S. where high heat flow and a shallow, very slow asthenosphere are observed, it is reasonable to infer that the negative *Sp* phases observed at 51 to 104 km (Figures 4, 9, and 10) do represent the LAB. Western U.S. LAB phases are in general larger than observed elsewhere on the continent and indicate velocity gradients that are localized over depth ranges of 30 km or less (assuming velocity drops of no more than 10%). Such velocity gradients cannot be explained solely by an increase in temperature from the lithosphere to the asthenosphere, unless localized mantle upwelling produces anomalously sharp vertical temperature variations. A more likely explanation is that western U.S. LAB velocity gradients reflect temperature in combination with asthenospheric partial melt and/or high asthenospheric hydration relative to drier lithosphere.

[61] In the portions of the eastern U.S. where observed negative *Sp* phases are interpreted as the LAB (Figures 6, 9, and 10), they imply LAB velocity gradients that occur over less than 30–40 km (for velocity drops of no more than 10%). Although the eastern U.S. *Sp* phases are in general weaker than in the western U.S, geodynamical models indicate that likely eastern U.S. thermal gradients will be too widely distributed in depth to produce the observed receiver functions, unless another factor, such as asthenospheric hydration or partial melt, sharpens the velocity contrast between lithosphere and asthenosphere.

[62] In contrast, the relatively thick (~200 km) high velocity lid imaged by surface and body wave tomography in cratonic North America and some sections of the Phanerozoic eastern U.S. leads to our interpretation of negative *Sp* phases at 59–113 km as a MLD. The origin of this layering internal to the lithosphere is still uncertain, but it could reflect alteration of the cratonic lithosphere by melt (for example, as the top of a melt cumulate zone) or it could represent the lower boundary of an ancient, highly depleted layer of lithosphere below which the rest of the cratonic lithosphere grew.

[63] The absence of a strong negative *Sp* phase at the base of the thickest North American lithosphere implies that its LAB velocity gradient is distributed over more than 50–70 km in depth. This gradient may be purely thermal in origin, although gradational changes in composition or melt content cannot be ruled out. Overall, these results indicate that the LAB is much more gradual in regions where the lithosphere is thicker than 150 km, compared to the sharper LAB velocity gradients observed in regions of thinner (<120 km) lithosphere.

[64] **Acknowledgments.** We thank Greg Hirth for very beneficial discussions, Scott Burdick for the mantle V_P model, Karin Sigloch for the subset of geological terrane boundaries from *Freeman and Johnson* [1946] used in Figure 1, and two anonymous reviewers for their helpful comments. Data were obtained from the IRIS Data Management Center. This work was funded by the NSF EarthScope Program under awards EAR-0641772 and EAR-0643060.

References

Ammon, C. J. (1991), The isolation of receiver effects from teleseismic P waveforms, *Bull. Seismol. Soc. Am.*, *81*, 2504–2510.

Anderson, D. L. (1989), *Theory of the Earth*, 366 pp., Blackwell, Malden, Mass.

Artemieva, I. M., and W. D. Mooney (2001), Thermal thickness and evolution of Precambrian lithosphere: A global study, *J. Geophys. Res.*, *106*, 16,387–16,414, doi:10.1029/2000JB900439.

Bassin, C., G. Laske, and G. Masters (2000), The current limits of resolution for surface wave tomography in North America, *Eos Trans. AGU*, *81*(48), Fall Meet. Suppl., F897.

Behn, M. D., and P. B. Kelemen (2006), Stability of arc lower crust: Insights from the Talkeetna arc section, south central Alaska, and the seismic structure of modern arcs, *J. Geophys. Res.*, *111*, B11207, doi:10.1029/2006JB004327.

Bennett, R. A., B. P. Wernicke, and J. L. Davis (1998), Continuous GPS measurements of contemporary deformation across the northern Basin and Range province, *Geophys. Res. Lett.*, *25*, 563–566, doi:10.1029/98GL00128.

Blackwell, D., J. L. Steele, and L. C. Carter (1991), Heat-flow patterns of the North American continent: A discussion of the geothermal map of North America, in *Neotectonics of North America*, edited by D. B. Slemmons, pp. 423–436, Geol. Soc. of Am., Boulder, Colo.

Bostock, M. G. (1998), Mantle stratigraphy and evolution of the Slave province, *J. Geophys. Res.*, *103*, 21,183–21,200, doi:10.1029/98JB01069.

Boyd, F. R. (1989), Compositional distinction between oceanic and cratonic lithosphere, *Earth Planet. Sci. Lett.*, *96*, 15–26, doi:10.1016/0012-821X(89)90120-9.

Burdick, S., C. Li, V. Martynov, T. Cox, J. Eakins, T. Mulder, L. Astiz, F. L. Vernon, G. L. Pavlis, and R. D. van der Hilst (2008), Upper mantle heterogeneity beneath North America from travel time tomography with global and USArray Transportable Array data, *Seismol. Res. Lett.*, *79*, 384–392, doi:10.1785/gssrl.79.3.384.

Cammarano, F., and B. Romanowicz (2007), Insights into the nature of the transition zone from physically constrained inversion of long-period seismic data, *Proc. Natl. Acad. Sci. U. S. A.*, *104*, 9139–9144, doi:10.1073/pnas.0608075104.

Carlson, R. W., D. G. Pearson, F. R. Boyd, S. B. Shirey, G. Irvine, A. H. Menzies, and J. J. Gurney (1999), Re-Os systematics of lithospheric peridotites: Implications for lithosphere formation and preservation, in *Proceedings of the Seventh International Kimberlite Conference*, B. J. Dawson Volume, edited by J. J. Gurney et al., pp. 99–108, Cape Town, South Africa.

Chen, L. (2009), Lithospheric structure variations between the eastern and central North China Craton from S- and P-receiver function migration, *Earth Planet. Sci. Lett.*, *173*, 216–277.

Chen, L., T. Y. Zheng, and W. W. Xu (2006), A thinned lithospheric image of the Tanlu Fault Zone, eastern China: Constructed from wave equation based receiver function migration, *J. Geophys. Res.*, *111*, B09312, doi:10.1029/2005JB003974.

Chulick, G. S., and W. D. Mooney (2002), Seismic structure of the crust and uppermost mantle of North America and adjacent ocean basins: A synthesis, *Bull. Seismol. Soc. Am.*, *92*, 2478–2492, doi:10.1785/0120010188.

Collins, J. A., F. L. Vernon, J. A. Orcutt, and R. A. Stephen (2002), Upper mantle structure beneath the Hawaiian swell: Constraints from the ocean seismic network pilot experiment, *Geophys. Res. Lett.*, *29*(11), 1522, doi:10.1029/2001GL013302.

Cook, F. A., A. J. Van der Velden, and K. W. Hall (1997), Upper mantle reflectors beneath the SNORCLE transect: Images of the base of the lithosphere?, in *Slave-Northern Cordillera Lithospheric Evolution (SNORCLE) Transect and Cordilleran Tectonics Workshop Meeting*, *Lithoprobe Rep. 56*, edited by F. Cook and P. Erdmer, pp. 58–62, Univ. of Calgary, Calgary, Alberta, Canada.

Cooper, C. M., A. Lenardic, and L. Moresi (2004), The thermal structure of stable continental lithosphere within a dynamic mantle, *Earth Planet. Sci. Lett.*, *222*, 807–817, doi:10.1016/j.epsl.2004.04.008.

Darbyshire, F. A., D. A. Eaton, A. W. Frederiksen, and L. Ertolahti (2007), New insights into the lithosphere beneath the Superior Province from Rayleigh wave dispersion and receiver function analysis, *Geophys. J. Int.*, *169*, 1043–1068, doi:10.1111/j.1365-246X.2006.03259.x.

Dasgupta, R., and M. M. Hirschmann (2006), Melting in the Earth's deep upper mantle caused by carbon dioxide, *Nature*, *440*, 659–662, doi:10.1038/nature04612.

Earle, P. S., and P. M. Shearer (1994), Characterization of global seismograms using an automatic-picking algorithm, *Bull. Seismol. Soc. Am.*, *84*, 366–376.

Eaton, D. W., F. Darbyshire, R. L. Evans, H. Grutter, A. G. Jones, and X. Yuan (2009), The elusive lithosphere-asthenosphere boundary beneath cratons, *Lithos*, *109*, 1–22, doi:10.1016/j.lithos.2008.05.009.

Elkins-Tanton, L. T., C. B. Till, and K. M. Fischer (2008), Melt could create a sharp lithosphere-asthenosphere boundary below eastern North America, *Eos Trans. AGU*, *89*(53), Fall Meet. Suppl., Abstract U43B-0066.

Farra, V., and L. Vinnik (2000), Upper mantle stratification by P and S receiver functions, *Geophys. J. Int.*, *141*, 699–712, doi:10.1046/j.1365-246x.2000.00118.x.

Faul, U. H., and I. Jackson (2005), The seismological signature of temperature and grain size variations in the mantle, *Earth Planet. Sci. Lett.*, *234*, 119–134, doi:10.1016/j.epsl.2005.02.008.

Faul, U. H., J. D. Fitz Gerald, and I. Jackson (2004), Shear wave attenuation and dispersion in melt-bearing olivine polycrystals: 2. Microstructural interpretation and seismological implications, *J. Geophys. Res.*, *109*, B06202, doi:10.1029/2003JB002407.

Fischer, K. M., H. A. Ford, D. L. Abt, and C. A. Rychert (2010), The lithosphere-asthenosphere boundary, *Annu. Rev. Earth Planet. Sci.*, *38*, 551–575, doi:10.1146/annurev-earth-040809-152438.

Ford, H. A., K. M. Fischer, D. L. Abt, L. T. Elkins-Tanton, and C. A. Rychert (2009), The lithosphere-asthenosphere boundary beneath Australia imaged by Sp phases, *Eos Trans. AGU*, *90*(52), Fall Meet. Suppl., Abstract DI11A-05.

Freeman, N. M., and D. W. Johnson (1946), Physiographic divisions of the conterminous U.S, U.S. Geol. Surv., Washington, D. C. (Available at http://water.usgs.gov/GIS/metadata/usgswrd/XML/physio.xml.)

French, S. W., K. M. Fischer, E. M. Syracuse, and M. E. Wysession (2009), Crustal structure beneath the Florida-to-Edmonton broadband seismometer array, *Geophys. Res. Lett.*, *36*, L08309, doi:10.1029/2008GL036331.

Gaherty, J. B., M. Kato, and T. H. Jordan (1999), Seismological structure if the upper mantle: A regional comparison of seismic layering, *Phys. Earth Planet. Inter.*, *110*, 21–41.

Godey, S., F. Deschamps, and J. Trampert (2004), Thermal and compositional anomalies beneath the North American continent, *J. Geophys. Res.*, *109*, B01308, doi:10.1029/2002JB002263.

Goes, S., and S. van der Lee (2002), Thermal structure of the North American uppermost mantle inferred from seismic tomography, *J. Geophys. Res.*, *107*(B3), 2050, doi:10.1029/2000JB000049.

Golub, G. H., M. Heath, and G. Wahba (1979), Generalized cross-validation as a method for choosing a good ridge parameter, *Technometrics*, *21*, 215–223, doi:10.2307/1268518.

Grand, S. P. (1994), Mantle shear structure beneath the Americas and surrounding oceans, *J. Geophys. Res.*, *99*, 11,591–11,621, doi:10.1029/94JB00042.

Grand, S. P. (2002), Mantle shear-wave tomography and the fate of subducted slabs, *Philos. Trans. R. Soc. London, Ser. B*, *360*, 2475–2491.

Grand, S. P., and D. V. Helmberger (1984), Upper mantle shear structure of North America, *Geophys. J. R. Astron. Soc.*, *76*, 399–438.

Gribb, T. T., and R. F. Cooper (2000), The effect of an equilibrated melt phase on the shear creep and attenuation behavior of polycrystalline olivine, *Geophys. Res. Lett.*, *27*, 2341–2344, doi:10.1029/2000GL011443.

Griffin, W. L., S. Y. O'Reilly, and C. G. Ryan (1999), The composition and origin of sub-continental lithospheric mantle, in *Mantle Petrology: Field Observations and High Pressure Experimentation: A Tribute to R. (Joe) Boyd*, pp. 13–45, Geochemical Society, Saint Louis, Mo.

Griffin, W. L., S. Y. O'Reilly, B. J. Doyle, N. J. Pearson, H. Coopersmith, K. Kivi, V. Malkovets, and N. Pokhilenko (2004), Lithosphere mapping beneath the North American plate, *Lithos*, *77*, 873–922, doi:10.1016/j.lithos.2004.03.034.

Grove, T. L., N. Chatterjee, S. W. Parman, and E. Médard (2006), The influence of H_2O on mantle wedge melting, *Earth Planet. Sci. Lett.*, *249*, 74–89, doi:10.1016/j.epsl.2006.06.043.

Gung, Y. C., M. Panning, and B. Romanowicz (2003), Global anisotropy and the thickness of continents, *Nature*, *422*, 707–711, doi:10.1038/nature01559.

Hales, A. L. (1969), A seismic discontinuity in the lithosphere, *Earth Planet. Sci. Lett.*, *7*, 44–46, doi:10.1016/0012-821X(69)90009-0.

Hammond, W. C., and E. D. Humphreys (2000), Upper mantle seismic wave velocity: Effects of realistic partial melt geometries, *J. Geophys. Res.*, *105*, 10,975–10,986, doi:10.1029/2000JB900041.

Hansen, S. E., A. J. Rodgers, S. Y. Schwartz, and A. M. S. Al-Amri (2007), Imaging ruptured lithosphere beneath the Red Sea and Arabian Peninsula, *Earth Planet. Sci. Lett.*, *259*, 256–265, doi:10.1016/j.epsl.2007.04.035.

Hansen, S. E., A. A. Nyblade, J. Julià, P. H. G. M. Dirks, and R. J. Durrheim (2009), Upper-mantle low-velocity zone structure beneath the Kaapval craton from *S*-wave receiver functions, *Geophys. J. Int.*, *178*, 1021–1027, doi:10.1111/j.1365-246X.2009.04178.x.

Heit, B., F. Sodoudi, X. Yuan, M. Bianchi, and R. Kind (2007), An S receiver function analysis of the lithospheric structure in South America, *Geophys. Res. Lett.*, *34*, L14307, doi:10.1029/2007GL030317.

Hirth, G., and D. L. Kohlstedt (1996), Water in the oceanic upper mantle: Implications for rheology, melt extraction and the evolution of the lithosphere, *Earth Planet. Sci. Lett.*, *144*, 93–108, doi:10.1016/0012-821X(96)00154-9.

Humphreys, E. D. (1995), Post-Laramide removal of the Farallon slab, western United States, *Geology*, *23*, 987–990, doi:10.1130/0091-7613(1995)023<0987:PLROTF>2.3.CO;2.

Humphreys, E. D., and K. G. Dueker (1994), Physical state of the western U.S. upper mantle, *J. Geophys. Res.*, *99*, 9635–9650, doi:10.1029/93JB02640.

Humphreys, E., E. Hessler, K. Dueker, G. L. Farmer, E. Erslev, and T. Atwater (2003), How Laramide-age hydration of North American lithosphere by the Farallon slab controlled subsequent activity in the western United States, *Int. Geol. Rev.*, *45*, 575–595, doi:10.2747/0020-6814.45.7.575.

Jordan, T. H. (1978), Composition and development of the continental tectosphere, *Nature*, *274*, 544–548, doi:10.1038/274544a0.

Jordan, T. H. (1988), Structure and formation of the continental tectosphere, *J. Petrol.*, spec. vol., *1*, 11–37.

Karato, S.-i., and H. Jung (1998), Water, partial melting and the origin of the seismic low velocity and high attenuation zone in the upper mantle, *Earth Planet. Sci. Lett.*, *157*, 193–207, doi:10.1016/S0012-821X(98)00034-X.

Karlstrom, K. E., and E. D. Humphreys (1998), Persistent influence of Proterozoic accretionary boundaries in the tectonic evolution of southwestern North America: Interaction of cratonic grain and mantle modification events, *Rocky Mountain Geology*, *33*, 161–179, doi:10.2113/33.2.161.

Katz, R. F., M. Spiegelman, and C. H. Langmuir (2003), A new parameterization of hydrous mantle melting, *Geochem. Geophys. Geosyst.*, *4*(9), 1073, doi:10.1029/2002GC000433.

Kawakatsu, H., P. Kumar, Y. Takei, M. Shinohara, T. Kanazawa, E. Araki, and K. Suyehiro (2009), Seismic evidence for sharp lithosphere-asthenosphere boundaries of oceanic plates, *Science*, *324*, 499–502.

Kennett, B. L. N. (1991), The removal free surface interactions from three-component seismograms, *Geophys. J. Int.*, *104*, 153–154, doi:10.1111/j.1365-246X.1991.tb02501.x.

Kennett, B. L. N., E. R. Engdahl, and R. Buland (1995), Constraints on seismic velocities in the Earth from travel-times, *Geophys. J. Int.*, *122*, 108–124, doi:10.1111/j.1365-246X.1995.tb03540.x.

King, S. D., and J. Ritsema (2000), African hot spot volcanism: Small-scale convection in the upper mantle beneath cratons, *Science*, *290*, 1137–1140, doi:10.1126/science.290.5494.1137.

Korenaga, J., and T. H. Jordan (2002), On the state of sublithospheric upper mantle beneath a supercontinent, *Geophys. J. Int.*, *149*, 179–189, doi:10.1046/j.1365-246X.2002.01633.x.

Kumar, P., X. Yuan, R. Kind, and G. Kosarev (2005a), The lithosphere-asthenosphere boundary in the Tien Shan-Karakoram region from S receiver functions: Evidence for continental subduction, *Geophys. Res. Lett.*, *32*, L07305, doi:10.1029/2004GL022291.

Kumar, P., et al. (2005b), The lithosphere-asthenosphere boundary in the north-west Atlantic region, *Earth Planet. Sci. Lett.*, *236*, 249–257, doi:10.1016/j.epsl.2005.05.029.

Kumar, P., X. Yuan, R. Kind, and J. Ni (2006), Imaging the colliding Indian and Asian lithospheric plates beneath Tibet, *J. Geophys. Res.*, *111*, B06308, doi:10.1029/2005JB003930.

Kumar, P., X. H. Yuan, M. R. Kumar, R. Kind, X. Q. Li, and R. K. Chadha (2007), The rapid drift of the Indian tectonic plate, *Nature*, *449*, 894–897, doi:10.1038/nature06214.

Lachenbruch, A. H. (1978), Heat-flow in Basin and Range and thermal effects of tectonic extension, *Pure Appl. Geophys.*, *117*, 34–50, doi:10.1007/BF00879732.

Langston, C. A. (1977), The effect of planar dipping structure on source and receiver responses for constant ray parameter, *Bull. Seismol. Soc. Am.*, *67*, 1029–1050.

Lee, C.-T. A. (2003), Compositional variation of density and seismic velocities in natural peridotites at STP conditions: Implications for seismic imaging of compositional heterogeneities in the upper mantle, *J. Geophys. Res.*, *108*(B9), 2441, doi:10.1029/2003JB002413.

Lekić, V., M. Panning, and B. Romanowicz (2010), A simple method for improving crustal corrections in waveform tomography, *Geophys. J. Int.*, *182*, 265–278, doi:10.1111/j.1365-246X.2010.04602.x.

Levin, V., and J. Park (1997), P-SH conversions in a flat-layered medium with anisotropy of arbitrary orientation, *Geophys. J. Int.*, *131*, 253–266, doi:10.1111/j.1365-246X.1997.tb01220.x.

Levin, V., and J. Park (2000), Shear zones in the Proterozoic lithosphere of the Arabian Shield and the nature of the Hales discontinuity, *Tectonophysics*, *323*, 131–148, doi:10.1016/S0040-1951(00)00105-0.

Li, C., R. D. van der Hilst, E. R. Engdahl, and S. Burdick (2008), A new global model for P wave speed variations in Earth's mantle, *Geochem. Geophys. Geosyst.*, *9*, Q05018, doi:10.1029/2007GC001806.

Li, X. D., and B. Romanowicz (1995), Comparison of global waveform inversions with and without considering cross-branch modal coupling, *Geophys. J. Int.*, *121*, 695–709, doi:10.1111/j.1365-246X.1995.tb06432.x.

Li, X., R. Kind, K. Priestley, S. V. Sobelev, F. Tillmann, X. Yuan, and M. Weber (2000), Mapping the Hawaiian plume conduit with converted seismic waves, *Nature*, *405*, 938–941, doi:10.1038/35016054.

Li, A., K. M. Fischer, S. van der Lee, and M. Wysession (2002), Crust and upper mantle discontinuity structure beneath eastern North America, *J. Geophys. Res.*, *107*(B5), 2100, doi:10.1029/2001JB000190.

Li, A., D. W. Forsyth, and K. M. Fischer (2003), Shear velocity structure and azimuthal anisotropy beneath eastern North America from Rayleigh wave inversion, *J. Geophys. Res.*, *108*(B8), 2362, doi:10.1029/2002JB002259.

Li, X., R. Kind, X. H. Yuan, I. Wolbern, and W. Hanka (2004), Rejuvenation of the lithosphere by the Hawaiian plume, *Nature*, *427*, 827–829, doi:10.1038/nature02349.

Li, X., X. Yuan, and R. Kind (2007), The lithosphere-asthenosphere boundary beneath the western United States, *Geophys. J. Int.*, *170*, 700–710, doi:10.1111/j.1365-246X.2007.03428.x.

Ligorria, J. P., and C. J. Ammon (1999), Iterative deconvolution and receiver-function estimation, *Bull. Seismol. Soc. Am.*, *89*, 1395–1400.

Lowry, A. R., M. Ribe, and R. B. Smith (2000), Dynamic elevation of the Cordillera, western United States, *J. Geophys. Res.*, *105*, 23,371–23,390, doi:10.1029/2000JB900182.

Marone, F., Y. C. Gung, and B. Romanowicz (2007), Three-dimensional radial anisotropic structure of the North American upper mantle from inversion of surface waveform data, *Geophys. J. Int.*, *171*, 206–222, doi:10.1111/j.1365-246X.2007.03465.x.

McKenzie, D., and M. J. Bickle (1988), The volume and composition of melt generated by extension of the lithosphere, *J. Petrol.*, *29*, 625–679.

McNamara, D. E., and T. J. Owens (1993), Azimuthal shear wave velocity anomaly in the basin and range province using Ps converted phases, *J. Geophys. Res.*, *98*, 12,003–12,017, doi:10.1029/93JB00711.

Médard, E., and T. L. Grove (2008), The effect of H2O on the olivine liquidus of basaltic melts: Experiments and thermodynamic models, *Contrib. Mineral. Petrol.*, *155*, 417–432, doi:10.1007/s00410-007-0250-4.

Mercier, J.-P., M. G. Bostock, P. Audet, J. B. Gaherty, E. J. Garnero, and J. Revenaugh (2008), The teleseismic signature of fossil subduction: Northwestern Canada, *J. Geophys. Res.*, *113*, B04308, doi:10.1029/2007JB005127.

Mierdel, K., H. Keppler, J. R. Smyth, and F. Langenhorst (2007), Water solubility in aluminous orthopyroxene and the origin of the Earth's asthenosphere, *Science*, *315*, 364–368, doi:10.1126/science.1135422.

Mohsen, A., R. Kind, S. V. Sobolev, M. Weber, and the DESERT Group (2006), Thickness of the lithosphere east of the Dead Sea Transform, *Geophys. J. Int.*, *167*, 845–852, doi:10.1111/j.1365-246X.2006.03185.x.

Morgan, P., and W. D. Gosnald (1989), Heat flow and thermal regimes in the continental United States, in *Geophysical Framework of the Continental United States*, *Geol. Soc. Am. Mem.*, vol. 172, edited by L. C. Pakiser and W. D. Mooney, pp. 129–161, Geol. Soc. of Am., Boulder, Colo.

Nagaya, M., H. Oda, H. Akazawa, and M. Ishise (2008), Receiver functions of seismic waves in layered anisotropic media: Application to the estimate of seismic anisotropy, *Bull. Seismol. Soc. Am.*, *98*, 2990–3006, doi:10.1785/0120080130.

Nettles, M., and A. M. Dziewonski (2008), Radially anisotropic shear velocity structure of the upper mantle globally and beneath North America, *J. Geophys. Res.*, *113*, B02303, doi:10.1029/2006JB004819.

Oreshin, S., L. Vinnik, D. Peregoudov, and S. Roecker (2002), Lithosphere and asthenosphere of the Tien Shan imaged by S receiver functions, *Geophys. Res. Lett.*, *29*(8), 1191, doi:10.1029/2001GL014441.

Ozacar, A. A., H. Gilbert, and G. Zandt (2008), Upper mantle discontinuity structure beneath East Anatolian Plateau (Turkey) from receiver functions, *Earth Planet. Sci. Lett.*, *269*, 427–435, doi:10.1016/j.epsl.2008.02.036.

Pearson, D. G., R. W. Carlson, S. B. Shirey, F. R. Boyd, and P. H. Nixon (1995), Stabilization of Archean lithospheric mantle: A Re-Os isotope study of peridotite xenoliths from the Kaapvaal craton, *Earth Planet. Sci. Lett.*, *134*, 341–357, doi:10.1016/0012-821X(95)00125-V.

Peltier, W. R., and R. Drummond (2008), Rheological stratification of the lithosphere: A direct inference based upon the geodetically observed pattern of the glacial isostatic adjustment of the North American continent, *Geophys. Res. Lett.*, *35*, L16314, doi:10.1029/2008GL034586.

Priestley, K., and D. McKenzie (2006), The thermal structure of the lithosphere from shear wave velocities, *Earth Planet. Sci. Lett.*, *244*, 285–301, doi:10.1016/j.epsl.2006.01.008.

Ramesh, D. S., R. Kind, and X. Yuan (2002), Receiver function analysis of the North American crust and upper mantle, *Geophys. J. Int.*, *150*, 91–108, doi:10.1046/j.1365-246X.2002.01697.x.

Ritsema, J., H. J. van Heijst, and J. H. Woodhouse (2004), Global transition zone tomography, *J. Geophys. Res.*, *109*, B02302, doi:10.1029/2003JB002610.

Rivers, T. (1997), Lithospheric elements of the Grenville Province: review and tectonic implications, *Precambrian Res.*, *86*, 117–154, doi:10.1016/S0301-9268(97)00038-7.

Romanowicz, B. (2009), The thickness of tectonic plates, *Science*, *324*, 474–476, doi:10.1126/science.1172879.

Roth, J. B., M. J. Fouch, D. E. James, and R. W. Carlson (2008), Three-dimensional seismic velocity structure of the northwestern United States, *Geophys. Res. Lett.*, *35*, L15304, doi:10.1029/2008GL034669.

Rychert, C. A., and P. M. Shearer (2009), A global view of the lithosphere-asthenosphere boundary, *Science*, *324*, 495–498, doi:10.1126/science.1169754.

Rychert, C. A., K. M. Fischer, and S. Rondenay (2005), A sharp lithosphere-asthenosphere boundary imaged beneath eastern North America, *Nature*, *436*, 542–545, doi:10.1038/nature03904.

Rychert, C. A., S. Rondenay, and K. M. Fischer (2007), *P*-to-*S* and *S*-to-*P* imaging of a sharp lithosphere-asthenosphere boundary beneath eastern North America, *J. Geophys. Res.*, *112*, B08314, doi:10.1029/2006JB004619.

Rychert, C. A., P. M. Shearer, and K. M. Fischer (2010), Scattered wave imaging of the lithosphere-asthenosphere boundary, *Lithos*, doi:10.1016/j.lithos.2009.12.006, in press.

Sacks, I. S., J. A. Snoke, and E. S. Husebye (1979), Lithosphere thickness beneath the Baltic shield, *Tectonophysics*, *56*, 101–110, doi:10.1016/0040-1951(79)90016-7.

Sato, H., I. S. Sacks, and T. Murase (1989a), The use of laboratory velocity data for estimating temperature and partial melt fraction in the low-velocity zone: Comparison with heat flow and electrical conductivity studies, *J. Geophys. Res.*, *94*, 5689–5704, doi:10.1029/JB094iB05p05689.

Sato, H., I. S. Sacks, T. Murase, G. E. Muncill, and H. Fukuyama (1989b), Qp-melting temperature relation in peridotite at high pressure and temperature: Attenuation mechanism and implications for the mechanical properties of the upper mantle, *J. Geophys. Res.*, *94*, 10,647–10,661, doi:10.1029/JB094iB08p10647.

Saul, J., M. R. Kumar, and D. Sarkar (2000), Lithospheric and upper mantle structure of the Indian Shield, from teleseismic receiver functions, *Geophys. Res. Lett.*, *27*, 2357–2360, doi:10.1029/1999GL011128.

Savage, B., and P. G. Silver (2008), Evidence for a compositional boundary within the lithospheric mantle beneath the Kalahari craton from S receiver functions, *Earth Planet. Sci. Lett.*, *272*, 600–609, doi:10.1016/j.epsl.2008.05.026.

Schutt, D. L., and C. E. Lesher (2006), Effects of melt depletion on the density and seismic velocity of garnet and spinel lherzolite, *J. Geophys. Res.*, *111*, B05401, doi:10.1029/2003JB002950.

Shapiro, S. S., B. H. Hager, and T. H. Jordan (1999), Stability and dynamics of the continental tectosphere, *Lithos*, *48*, 115–133, doi:10.1016/S0024-4937(99)00025-0.

Sleep, N. H. (2005), Evolution of the continental lithosphere, *Annu. Rev. Earth Planet. Sci.*, *33*, 369–393, doi:10.1146/annurev.earth.33.092203.122643.

Smith, W. H. F., and D. T. Sandwell (1997), Measured and estimated seafloor topography, *Boulder Res. Publ. RP-1*, http://www.ngdc.noaa.gov/mgg/fliers/97mgg03.html, World Data Cent. for Geophys. and Mar. Geol., Boulder, Colo.

Snyder, D. B. (2008), Stacked uppermost mantle layers within the Slave craton of NW Canada as defined by anisotropic seismic discontinuities, *Tectonics*, *27*, TC4006, doi:10.1029/2007TC002132.

Sodoudi, F., et al. (2006a), Lithospheric structure of the Aegean obtained from P and S receiver functions, *J. Geophys. Res.*, *111*, B12307, doi:10.1029/2005JB003932.

Sodoudi, F., X. Yuan, Q. Liu, R. Kind, and J. Chen (2006b), Lithospheric thickness beneath the Dabie Shan, central eastern China from S receiver functions, *Geophys. J. Int.*, *166*, 1363–1367, doi:10.1111/j.1365-246X.2006.03080.x.

Stixrude, L., and C. Lithgow-Bertelloni (2005), Mineralogy and elasticity of the oceanic upper mantle: Origin of the low-velocity zone, *J. Geophys. Res.*, *110*, B03204, doi:10.1029/2004JB002965.

Takei, Y. (2002), Effect of pore geometry on V-P/V-S: From equilibrium geometry to crack, *J. Geophys. Res.*, *107*(B2), 2043, doi:10.1029/2001JB000522.

Thybo, H. (2006), The heterogeneous upper mantle low velocity zone, *Tectonophysics*, *416*, 53–79, doi:10.1016/j.tecto.2005.11.021.

Thybo, H., and E. Perchuc (1997), The seismic 8° discontinuity and partial melt in the continental mantle, *Science*, *275*, 1626–1629, doi:10.1126/science.275.5306.1626.

van der Lee, S. (2002), High-resolution estimates of lithospheric thickness from Missouri to Massachusetts, USA, *Earth Planet. Sci. Lett.*, *203*, 15–23, doi:10.1016/S0012-821X(02)00846-4.

van der Lee, S., and G. Nolet (1997), Upper mantle S velocity structure of North America, *J. Geophys. Res.*, *102*, 22,815–22,838, doi:10.1029/97JB01168.

van der Lee, S., K. Regenauer-Lieb, and D. A. Yuen (2008), The role of water in connecting past and future episodes of subduction, *Earth Planet. Sci. Lett.*, *273*, 15–27, doi:10.1016/j.epsl.2008.04.041.

Vinnik, L. P. (1977), Detection of waves converted from P to SV in the mantle, *Phys. Earth Planet. lnter.*, *15*, 39–45.

Vinnik, L. P., V. Farra, and R. Kind (2004), Deep structure of the Afro-Arabian hotspot by S receiver functions, *Geophys. Res. Lett.*, *31*, L11608, doi:10.1029/2004GL019574.

Vinnik, L., E. Kurnik, and V. Farra (2005), Lehmann discontinuity beneath North America: No role for seismic anisotropy, *Geophys. Res. Lett.*, *32*, L09306, doi:10.1029/2004GL022333.

Wernicke, B., G. J. Axen, and J. K. Snow (1988), Basin and Range extensional tectonics at the latitude of Las Vegas, Nevada, *Bull. Seismol. Soc. Am.*, *100*, 1738–1757.

Wilson, D. C., D. A. Angus, J. F. Ni, and S. P. Grand (2006), Constraints on the interpretations of *S*-to-*P* receiver functions, *Geophys. J. Int.*, *165*, 969–980, doi:10.1111/j.1365-246X.2006.02981.x.

Wittlinger, G., and V. Farra (2007), Converted waves reveal a thick and layered tectosphere beneath the Kalahari super craton, *Earth Planet. Sci. Lett.*, *254*, 404–415, doi:10.1016/j.epsl.2006.11.048.

Wölbern, I., A. W. B. Jacob, T. A. Blake, R. Kind, X. Li, S. Yuan, F. Duennebier, and M. Weber (2006), Deep origin of the Hawaiian tilted plume conduit derived from receiver functions, *Geophys. J. Int.*, *166*, 767–781, doi:10.1111/j.1365-246X.2006.03036.x.

Xue, M., and R. M. Allen (2007), The fate of the Juan de Fuce plate: Implications for the Yellowstone plume head, *Earth Planet. Sci. Lett.*, *264*, 266–276, doi:10.1016/j.epsl.2007.09.047.

Yasuda, A., T. Fujii, and K. Kurita (1994), Melting phase relations of an anhydrous mid-ocean ridge basalt from 3 to 20 GPa: Implications for the behavior of subducted oceanic crust in the mantle, *J. Geophys. Res.*, *99*, 9401–9414, doi:10.1029/93JB03205.

Yuan, H., and B. Romanowicz (2010), Lithospheric layering in the North American craton, *Nature*, *466*, 1063–1068, doi:10.1038/nature09332.

Yuan, X., R. Kind, X. Li, and R. Wang (2006), The S receiver functions: Synthetics and data example, *Geophys. J. Int.*, *165*, 555–564, doi:10.1111/j.1365-246X.2006.02885.x.

Zandt, G., H. Gilbert, T. J. Owens, M. Ducea, J. Saleeby, and C. H. Jones (2004), Active foundering of a continental arc root beneath the southern Sierra Nevada in California, *Nature*, *431*, 41–46, doi:10.1038/nature02847.

Zhang, Q., E. Sandvol, and M. Liu (2009), Lithospheric velocity structure of the New Madrid Seismic Zone: A joint teleseismic and local P tomographic study, *Geophys. Res. Lett.*, *36*, L11305, doi:10.1029/2009GL037687.

Zhu, L.-P., and H. Kanamori (2000), Moho depth variation in southern California from teleseismic receiver functions, *J. Geophys. Res.*, *105*, 2969–2980, doi:10.1029/1999JB900322.

D. L. Abt, ExxonMobil Exploration Company, 222 Benmar Dr., CORP-GP8-710, Houston, TX 77060, USA. (david.l.abt@exxonmobil.com)

K. M. Fischer and H. A. Ford, Department of Geological Sciences, Brown University, P.O. Box 1846, Providence, RI 02912, USA.

S. W. French, Department of Earth and Planetary Science, University of California, 381 McCone Hall, Berkeley, CA 94720, USA.

B. Romanowicz and H. Yuan, Berkeley Seismological Laboratory, University of California, 209 McCone Hall, Berkeley, CA 94720, USA.